

4. THE TROPICS—H. J. Diamond, Ed.

a. Overview—H. J. Diamond

From the standpoint of the El Niño–Southern Oscillation (ENSO), indications are that ENSO-neutral conditions prevailed throughout the year, though mostly on the cool side of neutral.

Overall, global tropical cyclone (TC) activity during 2013 was slightly above average with a total of 94 storms (the 1981–2010 global average is 89), and was higher than in the previous three seasons, including 2010, which featured the lowest numbers of global TCs since the start of the satellite era (generally considered to have begun after 1970). Only the Western North Pacific Basin experienced above-normal activity in 2013; all other basins were either at or below normal levels. Globally, only four TCs reached the Saffir–Simpson hurricane wind scale Category 5 intensity level—three in the Western North Pacific Basin and one in the North Indian Ocean. This number of TCs (four) was just one more than the all-time lowest global number of Category 5 storms (recorded in both 2011 and 2012) since the Dvorak intensity estimation method was introduced in the 1980s (Diamond 2012).

This chapter consists of eight sections: (1) ENSO and the tropical Pacific; (2) tropical intraseasonal activity; (3) seasonal TC activity in the seven TC basins: the North Atlantic, Eastern North Pacific, Western North Pacific, North Indian and South Indian Oceans, Southwest Pacific, and Australia; (4) TC heat potential, which aids in summarizing the section for TCs from an ocean heat perspective; (5) global monsoon summary; (6) intertropical convergence zone behavior in the Pacific and Atlantic basins; (7) the Atlantic warm pool (AWP); and (8) the Indian Ocean dipole. The global monsoon summary section is new in response to feedback received for the inclusion of such a global summary. It is not intended to replace the more detailed monsoon descriptions included in the Regional Climates chapter. Finally, two sidebar articles detailing the unusually quiet North Atlantic hurricane season and the unique and destructive nature of the Western North Pacific Basin's Typhoon Haiyan are also included.

b. ENSO and the Tropical Pacific—G. D. Bell, M. L'Heureux, and M. Halpert

1) OCEANIC CONDITIONS

ENSO is a coupled ocean-atmosphere phenomenon over the tropical Pacific Ocean. Opposite phases of ENSO, El Niño and La Niña, are classified by NOAA's Climate Prediction Center (CPC) using the Niño-3.4 index, which is based on the area-averaged sea surface temperature (SST) anomalies in the east-central equatorial Pacific (5°N–5°S, 170°–120°W).

A time series of the weekly Niño-3.4 index for 2013 shows slightly cooler-than-average SSTs throughout the year, with departures generally in the range of -0.2° to -0.4°C (Fig. 4.1a). There were only three short periods in which the index became positive (early April, early September, and late November). The latter two periods were associated with the downwelling phases of equatorial oceanic Kelvin waves (see Fig. 4.7).

The Oceanic Niño index (ONI) is a three-month running average of the Niño-3.4 index, and is used by NOAA to monitor and predict ENSO and also to

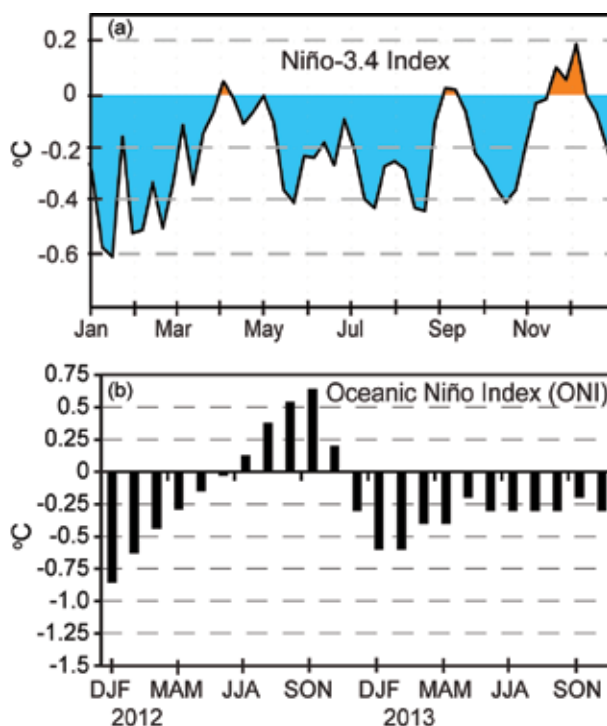


FIG. 4.1 Time series of (a) weekly SST anomalies ($^{\circ}\text{C}$) in the Niño-3.4 region (5°N–5°S, 170°W–120°W) and (b) the Oceanic Niño Index (ONI, $^{\circ}\text{C}$) from DJF 2012/13 through OND 2013. Values in (a) are departures from the 1981–2010 weekly adjusted OI climatology (Smith and Reynolds 1998). Values in (b) are derived from the ERSST-v3b dataset (Smith et al. 2008).

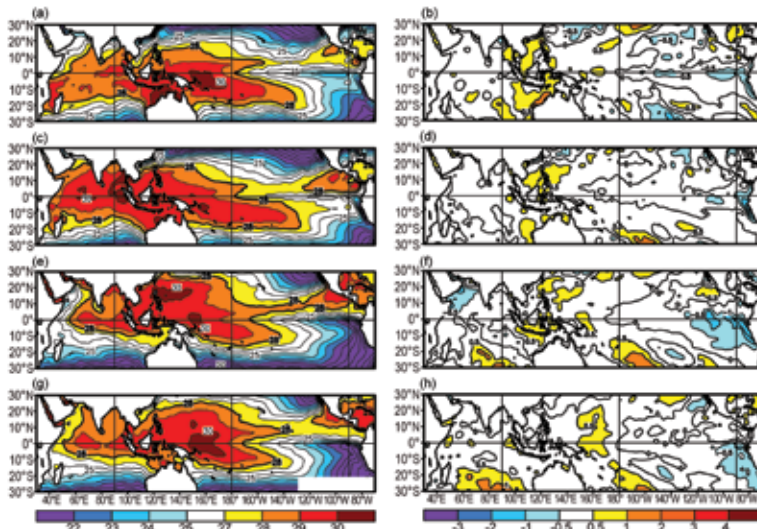


FIG 4.2. Seasonal SST (left) and anomaly (right) for (a, b) DJF 2012/13, (c, d) MAM 2013, (e, f) JJA 2013 and (g, h) SON 2013. Contour interval for total (anomalous) SST is 1°C (0.5°C). Anomalies are departures from the 1981–2010 seasonal adjusted OI SST climatology (Smith and Reynolds 1998).

classify ENSO events historically¹. A time series of the ONI shows values slightly cooler than -0.5°C early in the year, followed by values near -0.3°C for April–June (AMJ) though the end of the year (Fig. 4.1b). These values indicate ENSO-neutral conditions throughout the year, though mostly on the cool side of neutral.

The spatial structure and seasonal evolution of the tropical Pacific SSTs and anomalies during 2013 are shown in Fig. 4.2. Equatorial SSTs were slightly below average in the far eastern Pacific throughout the year, and above average in the far western Pacific especially during the latter part of the year (Fig. 4.2h). Consistent with these conditions, subsurface temperatures in the vicinity of the oceanic thermocline were above average west of the dateline throughout the year (Fig. 4.3), and below average in the eastern Pacific during December–February (DJF) 2012/13 through June–August (JJA) 2013 (Figs. 4.3b–d). Temperatures along the thermocline were also above average over the central equatorial Pacific during JJA and September–November (SON), reflecting a gradual build-up of oceanic heat content over the course of the year (Figs. 4.3c,d).

¹ For historical purposes, the CPC classifies an El Niño (La Niña) episode when the Oceanic Niño index (ONI) is greater (less) than or equal to $+0.5^{\circ}\text{C}$ (-0.5°C) for five consecutive overlapping seasons (as measured by the ERSST-v3b dataset, Smith et al. 2008); see http://www.cpc.ncep.noaa.gov/products/analysis_monitoring/ensostuff/ensoyears.shtml.

2) ATMOSPHERIC CIRCULATION

On the whole, near-average atmospheric wind and convection patterns reflected ENSO-neutral throughout the year (Figs. 4.4, 4.5). The main wind anomalies were found over the western equatorial Pacific during DJF through JJA, in association with anomalous low-level easterly winds (Figs. 4.4a–c) and anomalous upper-level southwesterly winds (Figs. 4.5a–c). This wind pattern was associated with enhanced convection over the Maritime Continent and far western equatorial Pacific, and with above-average SSTs in the western Pacific. In contrast, convection was slightly suppressed near the dateline during much of the year.

During JJA, the low-level circulation also featured anomalous westerly winds extending from the eastern sub-

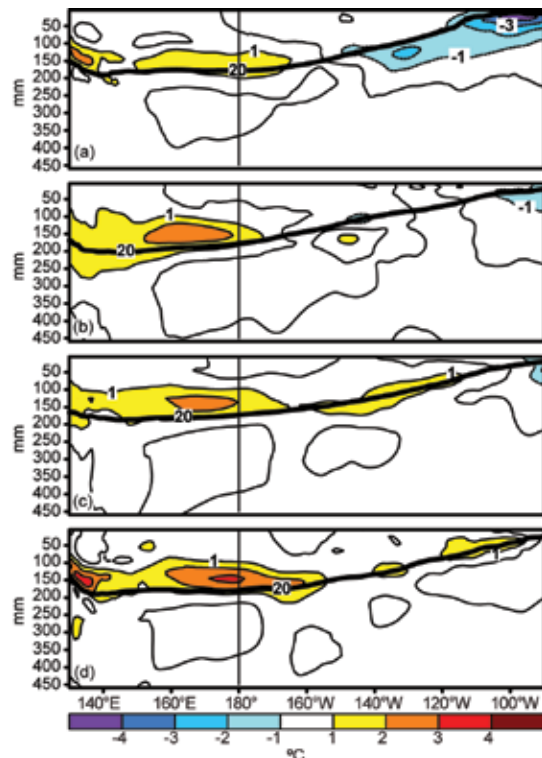


FIG 4.3. Equatorial depth-longitude section of ocean temperature anomalies ($^{\circ}\text{C}$) averaged between 5°N and 5°S during (a) DJF 2012/13, (b) MAM 2013, (c) JJA 2013, and (d) SON 2013. The 20°C isotherm (thick solid line) approximates the center of the oceanic thermocline. The data are derived from an analysis system that assimilates oceanic observations into an oceanic GCM (Behringer et al. 1998). Anomalies are departures from the 1981–2010 period monthly means.

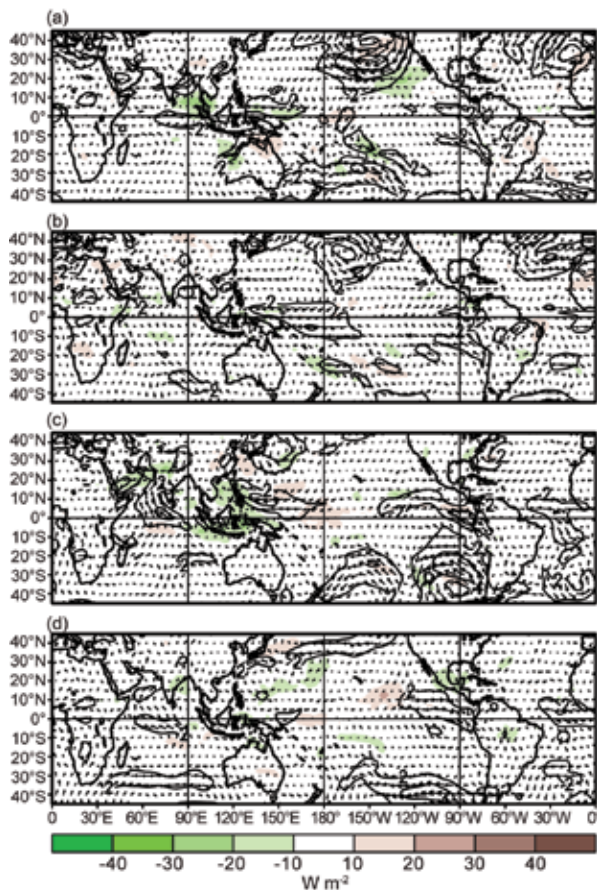


FIG. 4.4. Anomalous 850-hPa wind vectors and speed (contours, m s^{-1}), and anomalous OLR (shaded, W m^{-2}), during (a) DJF 2012/13, (b) MAM 2013, (c) JJA 2013, and (d) SON 2013. Anomalies are departures from the 1981–2010 period monthly means.

tropical North Pacific to equatorial western Africa (Fig. 4.4c). This pattern has been present since 1995 and is partly associated with the warm phase of the Atlantic multidecadal oscillation and concurrent enhancement of the west African monsoon system (G. D. Bell et al. 2011, 2013).

c. Tropical intraseasonal activity—S. Baxter, J. Gottschalck, and G. D. Bell

Tropical intraseasonal variability was prominent during 2013 in both the atmosphere and ocean. Three aspects of this variability included the Madden-Julian oscillation (MJO; Fig. 4.6; Madden and Julian 1971, 1972, 1994; Zhang 2005), atmospheric Kelvin and equatorial Rossby waves (Wheeler and Kiladis 1999; Wheeler and Weickmann 2001), and equatorial oceanic Kelvin wave activity (Fig. 4.7). There were three distinct periods of MJO activity, spanning a total of eight months. There were two distinct periods of nearly two months each (Fig. 4.6, blue boxes), dur-

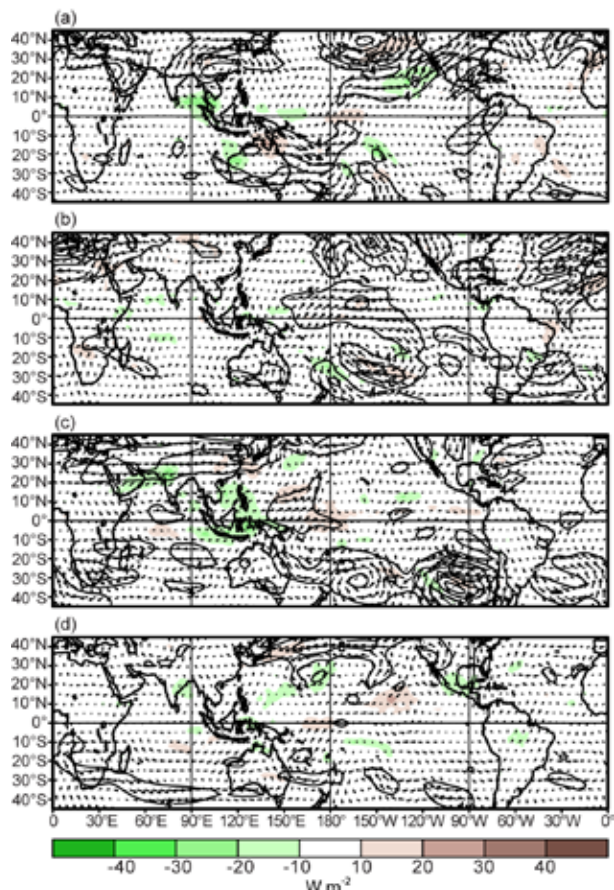


FIG. 4.5. Anomalous 200-hPa wind vectors and speed (contours, m s^{-1}), and anomalous OLR (shaded, W m^{-2}), during (a) DJF 2012/13, (b) MAM 2013, (c) JJA 2013, and (d) SON 2013. Anomalies are departures from the 1981–2010 period monthly means.

ing which rapidly propagating atmospheric Kelvin waves dominated the pattern of tropical convective variability. There were also three occurrences each of downwelling and upwelling oceanic Kelvin waves, collectively spanning nearly eight months.

The MJO is a leading climate mode of tropical convective variability that occurs on intraseasonal timescales. The convective anomalies associated with the MJO often have the same spatial scale as ENSO, but differ in that they exhibit a distinct eastward propagation and generally traverse the globe in 30–60 days. The MJO can strongly affect the tropical and extratropical atmospheric circulation patterns, and may produce ENSO-like anomalies on subseasonal timescales (Knutson and Weickmann 1987; Kiladis and Weickmann 1992; Mo and Kousky 1993; Kousky and Kayano 1994; Kayano and Kousky 1999; Riddle et al. 2012). The MJO is often quite variable in a given year, with periods of moderate-to-strong activity sometimes followed by little or no activity. Overall,

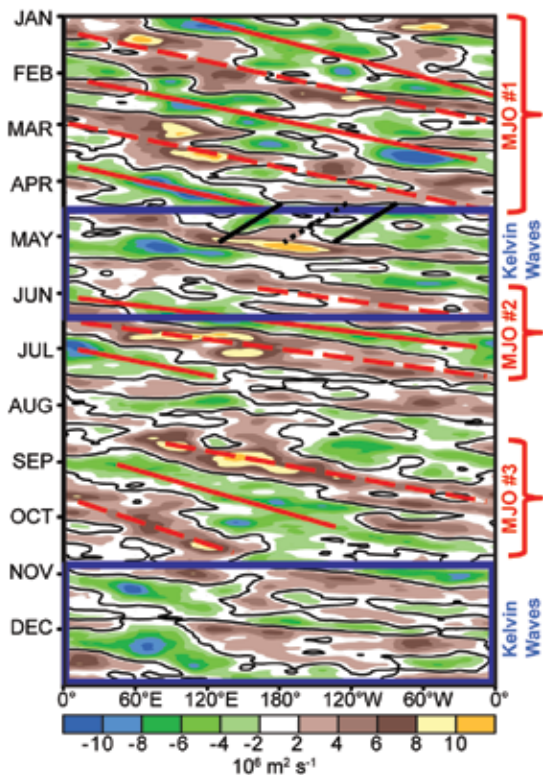


FIG. 4.6. Time-longitude section for 2013 of anomalous 200-hPa velocity potential ($\times 10^6 \text{ m}^2 \text{ s}^{-1}$) averaged between 5°N and 5°S . For each day, the period mean is removed prior to plotting. Green (brown) shading highlights likely areas of anomalous divergence and rising motion (convergence and sinking motion). Red lines and labels highlight the main MJO episodes. Blue boxes denote periods of atmospheric Kelvin wave activity discussed in text, and solid (dotted) black lines denote enhanced (suppressed) convective phases of an important equatorial atmospheric Rossby wave. Anomalies are departures from the 1981–2010 base period daily means.

the MJO tends to be most active during neutral and weak ENSO periods, and is often absent during strong El Niño events (Hendon et al. 1999; Zhang and Gottschalck 2002; Zhang 2005).

The MJO may be diagnosed as continuous eastward propagation of 200-hPa velocity potential anomalies around the globe. A time-longitude section of this parameter shows the three main MJO episodes during 2013 (Fig. 4.6), which included (1) a strong and long-lived episode from January to early April (MJO #1); (2) a strong, short-lived, and rapidly propagating episode from June to early July (MJO #2); and (3) a long-lived episode during much of September and October (MJO #3).

The first MJO episode (MJO #1) featured a zonal wave-1 pattern of strong convective anomalies and had a periodicity of approximately 45 days. Both the

enhanced convective phase (negative anomalies) and suppressed convective phase (positive anomalies) of this MJO propagated around the globe nearly three times. The event ended during April when westward-propagating atmospheric equatorial Rossby waves became the dominant feature (Fig. 4.6, black lines).

Some of the largest impacts from this prolonged MJO episode include the triggering of a downwelling oceanic Kelvin wave and interaction with the extratropics. The Kelvin wave was triggered during early February by a relaxation of the trade winds as enhanced convection propagated eastward across the Maritime Continent. This wave reached the eastern Pacific in March and resulted in a vastly decreased magnitude of negative upper-ocean heat content anomalies (Fig. 4.7).

The extratropical impacts from MJO #1 were most prominent in March and were associated with a combination of suppressed convection and anomalous upper-level convergence over the eastern Indian Ocean and anomalous upper-level divergence over the eastern Pacific Ocean. These conditions likely contributed to an eastward extension of the East Asian jet stream and to an intensifying negative phase of the Arctic Oscillation during March (See

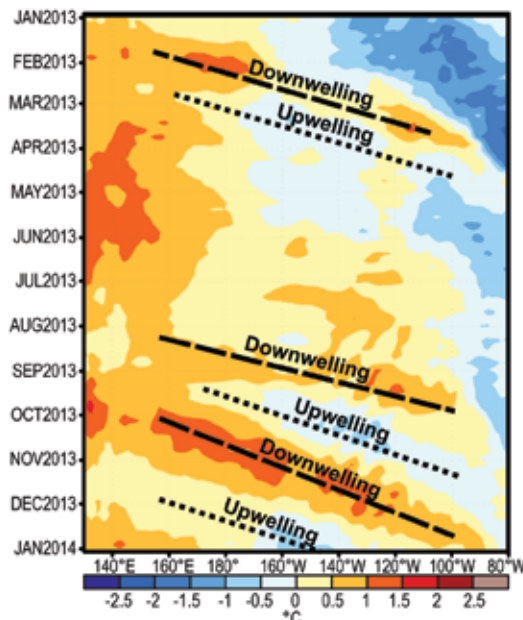


FIG. 4.7. Time-longitude section for 2013 of the anomalous upper Pacific Ocean (0–300 m) heat content averaged between 5°N and 5°S . Blue (yellow/red) shading indicates below (above) average heat content. The downwelling (dashed lines) and upwelling (dotted lines) phases of equatorial oceanic Kelvin waves are indicated. Anomalies are departures from the 1981–2010 base period pentad means.

Fig. A1.4; H. Lin et al. 2009; Cassou 2008), which had substantial extratropical impacts that included anomalously cold surface air temperatures during March across central Canada, the east-central United States, much of Europe, north west Russia, and parts of Japan (See Fig. A1.3).

This MJO was followed by a two-month period in which atmospheric Kelvin waves, indicated by a faster propagation of the velocity potential anomalies, were the prominent intraseasonal features in the tropical atmosphere (Fig. 4.6, blue boxes). The second MJO episode of 2013 (MJO #2, Fig. 4.6) began in June and ended in early July. As is common with many MJO episodes, its convective signal was partially masked by the atmospheric Kelvin wave activity, which resulted in a faster eastward propagation of the velocity potential anomalies (Roundy 2012; Sobel and Kim 2012). This MJO event exhibited phase speed on the high end of the MJO envelope, with a period of roughly 30 days.

The third MJO episode (MJO #3) of 2013 lasted from early September through late October, with a periodicity of approximately 50 days. In early and mid-September, the enhanced phase of this MJO propagated eastward across the western and central Pacific and the suppressed phase propagated across the Western Hemisphere. This configuration likely contributed to an uptick in tropical cyclone activity across the Western North Pacific Basin, while helping to suppress activity across the Eastern North Pacific and Atlantic Basins (Mo 2000; Klotzbach 2010). By mid-October the enhanced phase of this MJO had propagated across the tropical Atlantic Ocean but did little to enhance Atlantic TC activity. Other than June, this was the only instance during 2013 in which the MJO was conducive to Atlantic TC activity.

Also associated with MJO #3, enhanced convection over the western equatorial Pacific during October helped to weaken the trade winds and initiate a downwelling equatorial oceanic Kelvin wave similar to that associated with MJO #1. This wave was the strongest of the year and eventually reached the South American coast in late December (Fig. 4.7). During November and December, the tropical intraseasonal variability again featured a series of atmospheric Kelvin waves. Additionally during early November and again in early December, there were impressive bursts of convective activity over the Indian Ocean, which may have been triggered by the atmospheric Kelvin waves but subsequently exhibited little eastward propagation.

d. Tropical Cyclones

1) OVERVIEW—H. J. Diamond

The International Best Track Archive for Climate Stewardship (IBTrACS) comprises historical tropical cyclone (TC) best-track data from numerous sources around the globe, including all of the WMO Regional Specialized Meteorological Centers (RSMC; Knapp et al. 2010). To date, IBTrACS represents the most complete compilation of TC data and offers a unique opportunity to revisit the global climatology of TCs. Using IBTrACS data (Schreck et al. 2014, manuscript submitted to *Mon. Wea. Rev.*), a 30-year average value for storms (from WMO-based RSMC numbers) is noted for each basin.

The global tallying of total TC numbers is challenging and involves more than simply adding up basin totals because some storms cross basin boundaries, some basins overlap, and multiple agencies are involved in tracking and forecasting TCs. Compiling the activity (using WMO information) over all eight TC basins, the 2013 season (2012/13 in the Southern Hemisphere) had 94 named storms (wind speeds ≥ 34 kts or 18 m s^{-1}), which is slightly above the 1981–2010 average of 89, and the 2013 total was higher than the previous three seasons, with 2010 having the lowest number of global named storms since the start of the satellite era. The 2013 season also featured 50 hurricanes/typhoons/cyclones (HTC; wind speeds ≥ 64 kts or 33 m s^{-1}), which is also above the 1981–2010 average of 44 HTCs (Knapp et al. 2010). Of these, 14 (below the global average of 19) reached major HTC status (wind speeds ≥ 96 kts or 49 m s^{-1} ; WMO 2014).

There were four Category 5 systems during the year: Francisco, Lekima, and Haiyan (named Yolanda in the Philippines region) in the western North Pacific; and Phailin in the North Indian Ocean. This is one more Category 5 storm than during the previous two seasons in 2011 and 2012, which saw the lowest global number of Category 5 storms during the satellite era. However, there were several Category 3 and 4 intensity-level systems that had major impacts in 2013: (1) Evan, Freda, and Sandra in the southwest Pacific; (2) Lehar and Madi in the North Indian Ocean; (3) Danas, Utor, and Wipha in the western North Pacific; (4) Felleng in the South Indian Ocean; and (5) Rusty and Narelle in the Australian region.

The North Atlantic Basin season was unusually quiet despite the absence of El Niño conditions (see Sidebar 4.1 for more detailed information). The only basin with above-normal activity in 2013 was the Western North Pacific, which featured the most well-publicized and destructive storm of the year: Super

Typhoon Haiyan. The nature and climatology of Haiyan was unique and Sidebar 4.2 is included to better document this event.

- 2) ATLANTIC BASIN—G. D. Bell, C. W. Landsea, S. B. Goldenberg, R. J. Pasch, E. S. Blake, J. Schemm, and T. B. Kimberlain

(i) 2013 Seasonal activity

The 2013 Atlantic hurricane season produced 13 named storms, of which only 2 became hurricanes, and none became major hurricanes. The HURDAT2 1981–2010 seasonal averages are 11.8 tropical storms, 6.4 hurricanes, and 2.7 major hurricanes (Landsea and Franklin 2013). The 2013 season ties 1982 for the fewest hurricanes in the recent historical record from 1950 to present, and is the first season since 1994 with no major hurricanes. The entire life cycle of both hurricanes occurred within the period of 9–16 September.

The seasonal accumulated cyclone energy (ACE) value (Bell et al. 2000) was only 39% of the 1981–2010 median (Fig. 4.8)². This is the 10th lowest value since records began in 1950 and satisfies NOAA’s criteria for a below-normal season (see http://www.cpc.ncep.noaa.gov/products/outlooks/background_information.shtml).

The 2013 ACE value, as well as the numbers of hurricanes and major hurricanes, are the lowest of the current high-activity era for Atlantic hurricanes that began in 1995 (Landsea et al. 1998; Goldenberg et al. 2001; Bell and Chelliah 2006; Bell et al. 2013). Thirteen seasons since 1995 (68%) have been above normal and only three (16%) have been below normal. Only one of these below-normal seasons (2013) occurred in the absence of El Niño, which is an indicator of how unusual the 2013 season was. In fact, the 2013 values for every parameter (except number of named storms) were below 1997, a year with one of the strongest El Niños in over 50 years. More details on the unusually quiet 2013 season can be found in Sidebar 4.1.

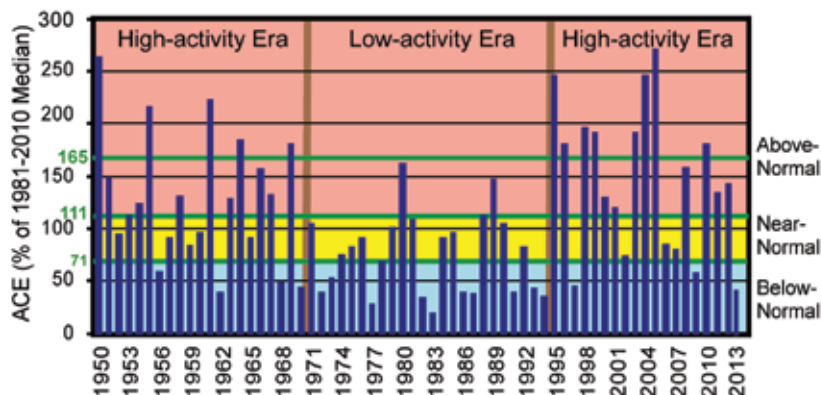


FIG. 4.8. NOAA's Accumulated Cyclone Energy (ACE) index expressed as percent of the 1981–2010 median value. ACE is calculated by summing the squares of the 6-hourly maximum sustained wind speed (knots) for all periods while the storm is at least tropical storm strength. Pink, yellow, and blue shadings correspond to NOAA's classifications for above-, near-, and below-normal seasons, respectively. The 165% threshold for a hyperactive season is indicated. Vertical brown lines separate high- and low-activity eras.

A main delineator between above- and below-normal seasons (Fig. 4.9) is the frequency of hurricanes and major hurricanes that originate as named storms within the main development region [MDR; green boxed region in Fig. 4.10a, which encompasses the tropical Atlantic Ocean and Caribbean Sea between 9.5° and 21.5°N (Goldenberg et al. 2001; Bell and Chelliah 2006)]. Only six named storms formed in the MDR during 2013, producing one hurricane (Humberto) and having a total ACE value that was 18% of the median. These numbers are comparable to the average MDR activity of a below-normal season,

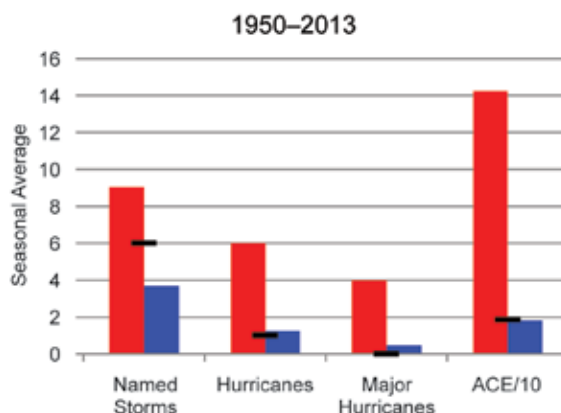


FIG. 4.9. Seasonal activity associated with storms first named in the Atlantic MDR. Red bars show the averages for above-normal seasons, blue bars show the averages for below-normal seasons, and black lines show the 2013 MDR activity. Season classifications are based on NOAA's criteria (see http://www.cpc.ncep.noaa.gov/products/outlooks/background_information.shtml).

² ACE is calculated by summing the squares of the six-hourly maximum sustained wind speed (knots) for all periods while the storm is at least tropical storm strength.

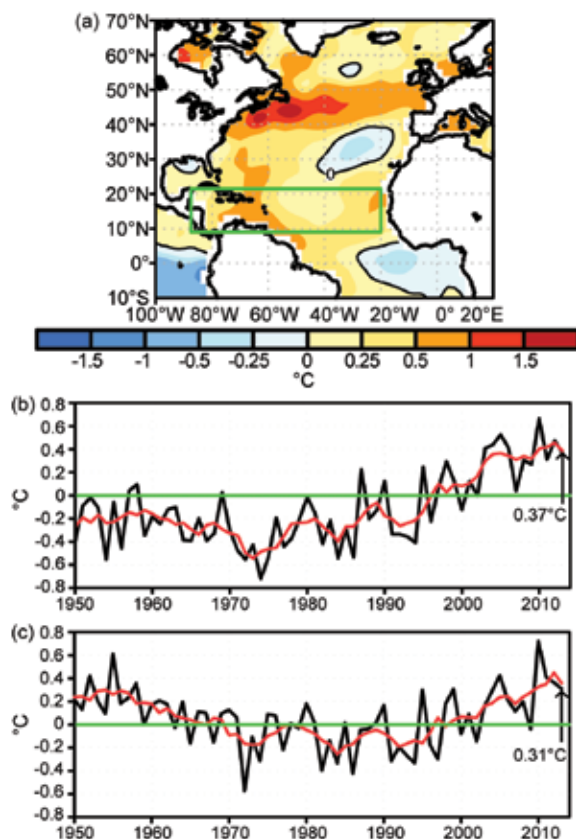


FIG. 4.10. (a) ASO 2013 SST anomalies (°C). (b) Time series during 1950–2013 of ASO area-averaged SST anomalies in the MDR [green box in (a)]. (c) Time series showing the difference between ASO area-averaged SST anomalies in the MDR and those for the entire global tropics (20°N–20°S). Red lines show a 5-pt. running mean of each time series. Anomalies are departures from the ERSST-v3b (Smith et al. 2008) 1981–2010 period monthly means.

and are at least six times lower than the above-normal season averages (six hurricanes and an ACE value of 142% of the median).

(ii) Storm Tracks

The 2013 Atlantic hurricane season featured three distinct sets of storm tracks. The first was related to five named storms that formed over the central and eastern tropical and subtropical Atlantic. Only one of these storms made landfall—Tropical Storm Chantal in the Caribbean islands. The second set of tracks reflected three named storms that formed in the Bay of Campeche and made landfall in eastern Mexico. Of these storms, Ingrid was the only hurricane of the season to make landfall. The third set of tracks reflected two tropical storms that moved across the central Gulf of Mexico. One of these systems, Tropical Storm Andrea, was the first named storm of the

season and the only U.S. landfalling storm, striking northwestern Florida before moving across south-eastern Georgia and South Carolina and becoming extratropical in North Carolina.

(iii) Atlantic sea surface temperatures

SSTs in the MDR were above average during the peak months (August–October, ASO) of the season, with the largest departures (between +0.5° and +1.0°C) observed across the eastern half of the Caribbean Sea (Fig. 4.10a). The mean SST departure within the MDR was +0.37°C. This value is the seventh highest in the 1950–2013 record (Fig. 4.10b) and is 0.3°C warmer than the average departure for the entire global tropics (Fig. 4.10c). This relative warmth within the MDR has been present since 1995 and is a feature of the warm phase of the Atlantic multidecadal oscillation (AMO; Enfield and Mestas-Núñez 1999; Goldenberg et al. 2001; G. D. Bell et al. 2011, 2013), and this makes the relative inactivity for the season all the more unusual.

(iv) Atmospheric circulation

The below-normal Atlantic hurricane season was largely the result of a set of exceptionally non-conductive atmospheric conditions within the MDR. One suppressing factor was the presence of strong ($\geq 8 \text{ m s}^{-1}$) 200–850 hPa vertical wind shear across most of the tropical Atlantic Ocean, Caribbean Sea, and Gulf of Mexico (Fig. 4.11), with above-average shear observed across the Caribbean Sea and Gulf of Mexico (not shown). Areas of weaker shear were confined to the southeastern MDR and Bay of Campeche. This signal is in stark contrast to a typical above-normal season, which features weak shear across large portions of the MDR.

Also during ASO 2013, large areas within the MDR experienced anomalous upper-level conver-

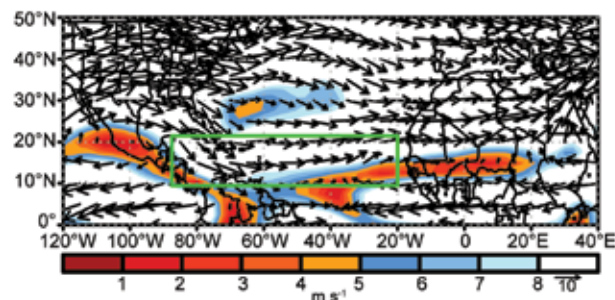


FIG. 4.11. ASO 2013 vertical wind shear magnitude and vectors (m s^{-1}). Shading indicates areas where the vertical wind shear magnitude is $\leq 8 \text{ m s}^{-1}$. Green box denotes the MDR. Vector scale is below right of color bar.

gence and lower-level divergence (Fig. 4.12a), along with anomalous mid- and low-level sinking motion (Fig. 4.12b) and drier air (Fig. 4.12c). None of these conditions are conducive to TC formation. Furthermore, the conducive phase of the MJO (Mo 2000) did not substantially offset these non-conductive conditions since it was present for only a brief period in early September and mid-October (see Fig. 4.6).

Climate factors such as El Niño and the cold phase of the AMO can produce non-conductive conditions within the MDR, but neither of these factors were present during ASO 2013. Instead, the observed conditions were related to a strong and persistent anomalous 200-hPa wave pattern that extended from North America to the eastern North Atlantic (Fig. 4.13a). This wave pattern had no apparent large-scale climate links. Key features of this pattern (ridge and trough axes shown by thick black lines in Fig. 4.13c) include: (1) an amplified ridge extending northward from Mexico; (2) a downstream amplified trough over the western subtropical North Atlantic and Caribbean Sea (called the tropical upper-tropospheric trough, TUTT); and (3) an amplified ridge over the central and eastern subtropical North Atlantic.

This wave pattern contributed to the non-conductive conditions within the MDR in two primary ways. First, its associated northwesterly flow from the Great Lakes to the southern Caribbean Sea (Fig. 4.13a) produced anomalous northerly and northwesterly vertical wind shear across the entire Caribbean Sea, resulting in the anomalously strong shear observed across the western half of the MDR (Fig. 4.13b).

Second, the strong curvature of the wave pattern was likely the primary contributor to the anomalous upper-level convergence and sinking motion across

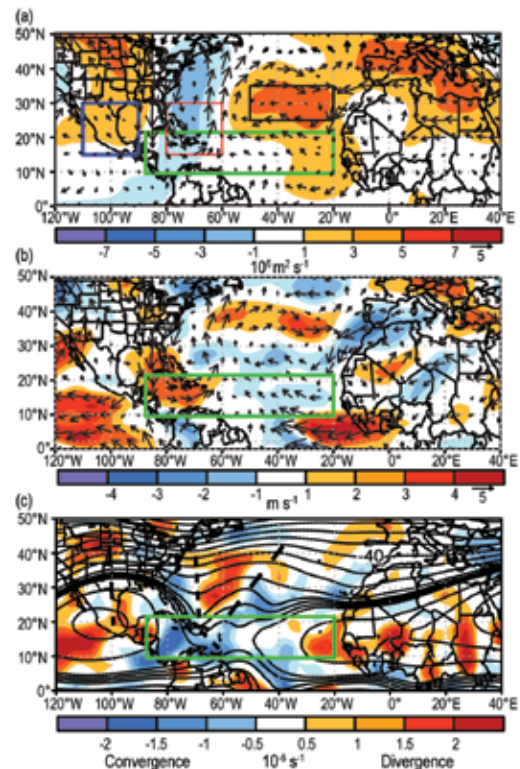


FIG. 4.13. ASO 2013 circulation and anomalies: (a) 200-hPa anomalous streamfunction (shaded, $\times 10^{-6} \text{ m}^2 \text{ s}^{-1}$) and wind vector (m s^{-1}), (b) 200 hPa–850 hPa anomalous magnitude of vertical wind shear and anomalous shear vector (m s^{-1}), and (c) total 200-hPa streamfunction (contours, interval is $5 \times 10^6 \text{ m}^2 \text{ s}^{-1}$, with additional solid contours at an interval of $1 \times 10^6 \text{ m}^2 \text{ s}^{-1}$) and anomalous divergence (shaded, $\times 10^{-6} \text{ s}^{-1}$). Boxes in (a) show index regions for Figs. 4.14 and 4.15. Vector scales for (a, b) are shown below right of color bar. Thick dashed lines in (c) identify ridge and trough axes of persistent wave pattern discussed in text. Green boxes in all panels indicate the MDR. Anomalies are based on the 1981–2010 climatology.

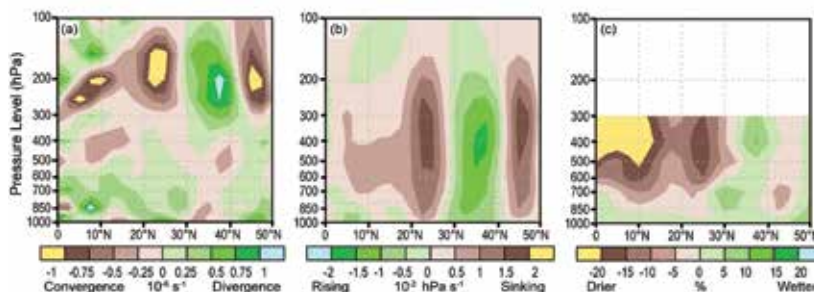


FIG. 4.12. Aug–Oct 2013 height-latitude sections averaged between 40°W – 60°W of (a) anomalous divergence ($\times 10^6 \text{ s}^{-1}$), (b) anomalous vertical velocity ($\times 10^{-2} \text{ Pa s}^{-1}$), and (c) percent of normal specific humidity. Green shading indicates anomalous divergence, anomalous rising motion, and increased moisture, respectively. Brown shading indicates anomalous convergence, anomalous sinking motion, and decreased moisture. Climatology and anomalies are with respect to the 1981–2010 period monthly means.

the western and central MDR. This area was part of a much larger region of upper-level convergence located between the amplified ridge (over Mexico) and the downstream TUTT axis, which is an area within midlatitude wave patterns known for upper-level convergence and descending motion. Similarly, a strong ridge within the eastern portion of the wave pattern contributed to the anomalous upper-level convergence and sinking motion over the central MDR, and also over the central subtropical North Atlantic north of the MDR.

Given these relationships, it is of interest to quantify the relative strength of the 200-hPa wave pattern during ASO 2013, along with its historical frequency of occurrence. The analysis is based upon ASO standardized streamfunction indices for the three regions shown in Fig. 4.13a [Mexico (blue box), the Caribbean Sea and western subtropical North Atlantic (orange box), and the eastern North Atlantic (black box)].

The index time series (dating back to 1970) shows that streamfunction anomalies within the Caribbean Sea region (Fig. 4.14, orange bars) typically have the same sign as those in both the Mexico (Fig. 4.14a, blue bars) and east Atlantic (Fig. 4.14b, black bar) regions. These relationships are reflected in their strong index correlations (0.86 and 0.73, respectively). In contrast, the ASO 2013 anomalies in the Caribbean Sea region had an opposite sign of the other two regions. There is only one other instance in the record (the below-normal 1994 season which featured three hurricanes, no major hurricanes, and an ACE of 35% of the me-

dian) in which a similar wave pattern existed with the amplitudes of all three indices exceeding 0.25 standard deviations.

An examination of the differences in index amplitudes between the three regions shows that the ASO 2013 wave pattern was of record strength (Figs. 4.15a,b). Similarly, the standardized index that is the sum of the anomaly differences from Figs. 4.15a and b (Fig. 4.15c) was also of record strength (+3 standard deviations), exceeding the next largest value (+2 standard deviations during ASO 1994) by a full standard deviation.

The analysis shows that the exceptionally non-conductive conditions within the MDR during ASO 2013 were linked to a rare (only twice since 1970) upper-level wave pattern of record strength that extended from Mexico to the eastern North Atlantic. It is of note that El Niño was present when this pattern last occurred in ASO 1994, but this was not the case during 2013.

This wave pattern does not have a known relationship to other climate factors and it therefore has a low probability of prediction on seasonal time scales.

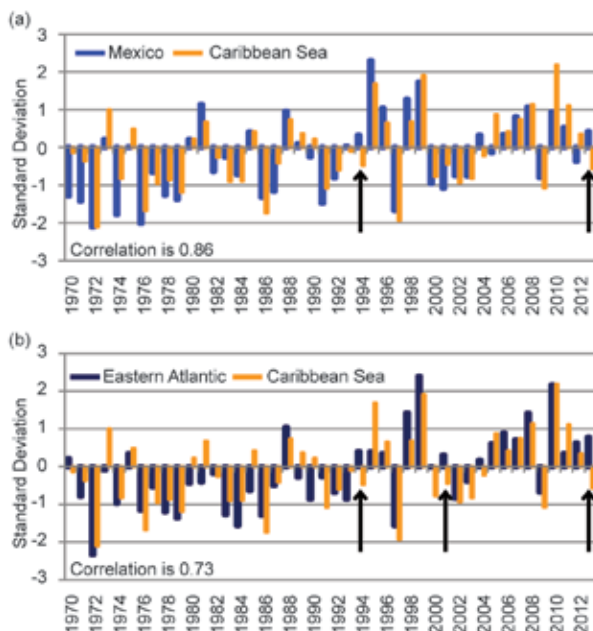


FIG. 4.14. ASO standardized streamfunction indices for the period 1970–2013 averaged over the boxed regions shown in Fig. 4.13a. Panel (a) shows indices for the Mexico (blue) and Caribbean Sea (orange) regions and panel (b) shows indices for the eastern Atlantic (black) and Caribbean Sea (orange) regions. The indices are calculated by first standardizing the ASO streamfunction anomalies at each grid point, and then standardizing the area-averaged value of the standardized grid-point anomalies. The correlations between the Mexico and Caribbean Sea indices and between the Eastern Atlantic and Caribbean Sea indices are given in panels (a) and (b), respectively. All standardizations are based on the 1981–2010 climatology.

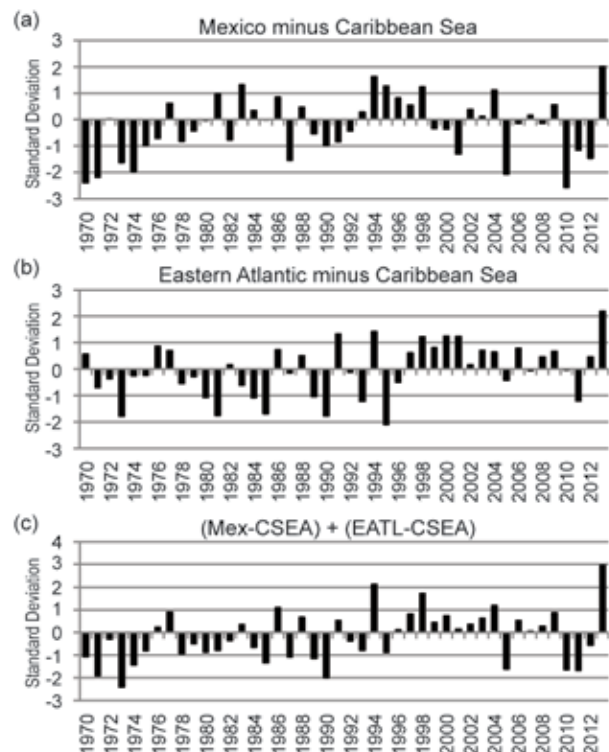


FIG. 4.15. ASO standardized indices for the period 1970–2013 based on (a) the Mexico minus Caribbean Sea indices from Fig. 4.14a, panel (b) the east Atlantic minus the Caribbean Sea indices from Fig. 4.14b, and (c) the indices in panel (a) minus those in (b). All standardizations are based on the 1981–2010 climatology.

Based on this analysis and on the ongoing warm phase of the AMO, the suppressed 2013 Atlantic hurricane season provides no indication that the current high-activity era for Atlantic hurricanes has ended.

3) EASTERN NORTH PACIFIC AND CENTRAL NORTH PACIFIC BASINS—M. C. Kruk, C. J. Schreck, and T. Evans

(i) Seasonal activity

The Eastern North Pacific (ENP) Basin is officially split into two separate regions for the issuance of warnings and advisories by NOAA's National Weather Service. NOAA's National Hurricane Center is responsible for issuing warnings in the eastern part of the basin that extends from the Pacific Coast of North America to 140°W, while NOAA's Central Pacific Hurricane Center in Honolulu, Hawaii, is responsible for issuing warnings in the central North Pacific (CNP) region between 140°W and the dateline. This section summarizes the TC activity in both warning areas using combined statistics, along with information specifically addressing the observed activity and impacts in the CNP region.

The ENP/CNP hurricane season officially spans from 15 May to 30 November. Hurricane and tropical storm activity in the eastern area of the basin typically peaks in September, while in the central Pacific TC activity normally reaches its seasonal peak in August (Blake et al. 2009). During the 2013 season, a total of 20 named storms formed in the combined ENP/CNP Basin, with only 2 of these forming in the CNP (very close to the dateline). This total included nine hurricanes and one major hurricane. The 1981–2010 IB-TrACS seasonal averages for the basin are 16.5 named storms, 8.5 hurricanes, and 4.0 major hurricanes.

An above-normal number of five named storms developed or entered into the CNP during 2013 (Fig. 4.16). Although half the TCs that formed in 2013 reached hurricane intensity, the ACE index for 2013 indicates many of the storms were weak and short-lived, with a seasonal value of only $70.1 \times 10^4 \text{ kt}^2$ (Fig. 4.16), which is well below the 1981–2010 mean of $137.0 \times 10^4 \text{ kt}^2$ (Bell et al. 2000; Bell and Chelliah 2006).

(ii) Environmental influences on the 2013 season

Figure 4.17 illustrates the background conditions for TC activity in the ENP and CNP during 2013. Consistent with the marginal La Niña conditions, weak cool SST anomalies were observed near the equator and along the Central American coast (Fig. 4.17a). Most of the TCs formed over an area of warm SST anomalies to the north off the Mexican coast. This also coincided with a broad region of enhanced

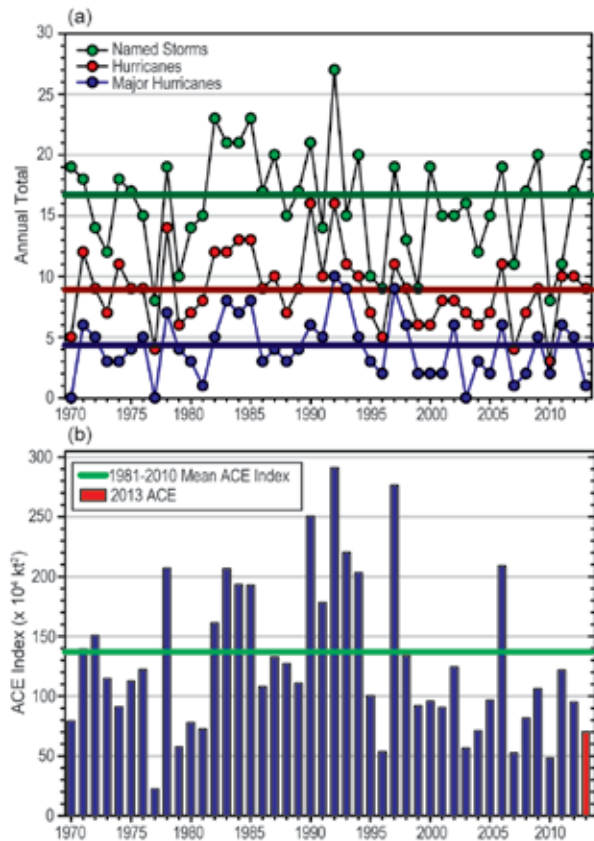


FIG. 4.16. Seasonal TC statistics for the ENP basin over the period 1970–2013: (top) number of named storms, hurricanes, and major hurricanes, and (bottom) the ACE Index ($\times 10^4 \text{ kt}^2$) with the seasonal total of 2013 highlighted in red. The time series shown includes the corresponding 1981–2010 base period means for each parameter.

convection that extended from 140°W eastward to the Gulf of Mexico (Fig. 4.17b). Meanwhile, the ITCZ was generally suppressed and shifted northward, as indicated by the positive outgoing longwave radiation (OLR) anomalies along 5°N and negative anomalies near 12°N. Vertical wind shear magnitudes were generally close to their climatological values (Fig. 4.17c); however, the vertical wind shear anomalies were generally easterly in the ENP, which might have also favored cyclogenesis.

Figure 4.17d shows a broad area of 850-hPa westerly anomalies near the equator, with easterly anomalies to the north, similar to what occurred in 2012 (Diamond 2013). This combination produced the region of enhanced cyclonic vorticity within which most of the ENP storms developed. Many of these storms developed where the enhanced vorticity intersected the westerly anomalies. The westerlies could have strengthened easterly wave activity in this region through barotropic energy conversion

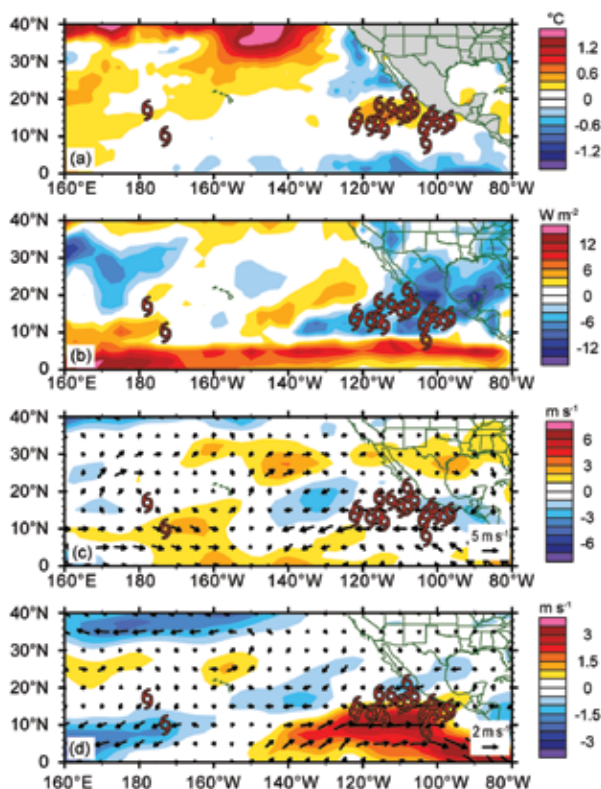


FIG. 4.17. Maps of May–Nov 2013 anomalies of (a) SST, (b) OLR, (c) 850–200-hPa vertical wind shear vector (arrows) and scalar (shading) anomalies, and (d) 850-hPa winds (arrows) and zonal wind (shading) anomalies. Anomalies are relative to the annual cycle from 1981–2010, except for SST which is relative to 1982–2010 due to data availability. Hurricane symbols denote where each ENP TC attained tropical storm intensity. Wind data are obtained from the NCEP–DOE Reanalysis 2 (Kanamitsu et al. 2002).

and wave accumulation (Maloney and Hartmann 2001; Aiyer and Molinari 2008). During 2013, these westerlies were also associated with a persistent upper level trough off the coast of Baja California that helped steer many of the TCs to make landfall in that region (Farfán et al. 2012).

ENP TC activity is strongly influenced by the MJO (Maloney and Hartmann 2001; Aiyer and Molinari 2008; Slade and Maloney 2013) and recent studies have found a greater role for convectively coupled Kelvin waves in modulating tropical cyclogenesis (Schreck and Molinari 2012; Ventrice et al. 2012a,b). Figure 4.18 uses OLR to examine the evolution of convection during the 2013 ENP hurricane season. Following Kiladis et al. (2005, 2009), the black contours identify the MJO-filtered anomalies and the green contours are filtered for Kelvin waves. Easterly waves are also apparent in the unfiltered anomalies (shading) as westward moving features, such as the

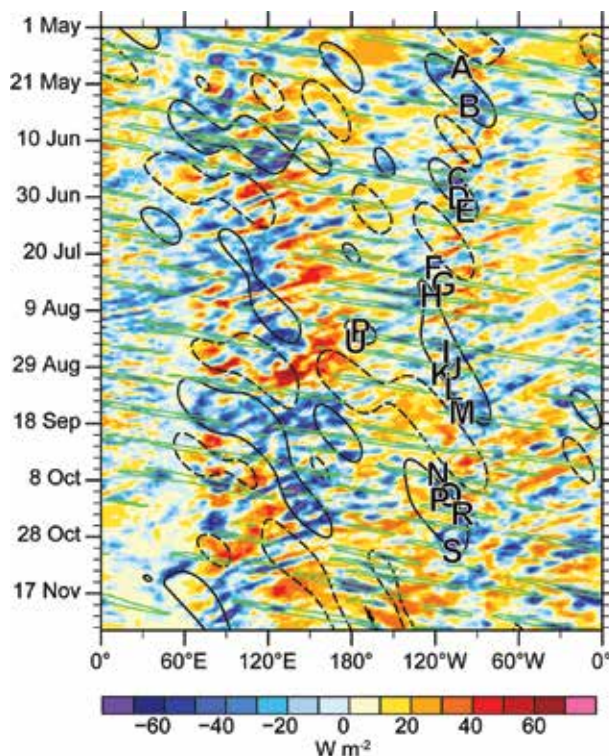


FIG. 4.18. Longitude-time Hovmöller of OLR averaged 10°N–20°N. Unfiltered anomalies from a daily climatology are shaded. Black contours denote MJO-filtered anomalies at +10 W m^{-2} (dashed) and -10 W m^{-2} (solid). Kelvin-filtered anomalies are contoured in green at -10 W m^{-2} . Letters indicate the genesis of ENP TCs.

ones leading up to Tropical Storm Juliette and Hurricane Manuel.

The MJO played a dominant role in modulating ENP TC activity during 2013. Nearly every ENP TC developed within periods of active MJO convection over the ENP associated with an MJO (black solid contours) that could be traced back to signals in the western North Pacific (WNP). The suppressed phases of the MJO (black dashed contours) are also consistent with the quiet periods in early June, early July, and late September. The only storms that were not clearly associated with the MJO were Tropical Storm Flossie and Hurricanes Gil and Henriette, which were the only three storms of the season to traverse from the ENP to the CNP.

Tropical Storms Pewa and Unala in the CNP are of particular interest as both storms appear to have developed in association with a Kelvin wave (green contours) that connected the dissipating MJO in the WNP with the intensifying convection in the ENP. Such a connection is consistent with recent studies that have found that the MJO often transitions to a Kelvin-like structure in the Western Hemisphere (Straub et al. 2006; Sobel and Kim 2012).

(iii) TC impacts

During the 2013 season, 9 of the season's 20 combined ENP/CNP tropical storms affected the western coast of Mexico and Baja California. The long-term annual average number of landfalling storms onto the western coast of Mexico is 1.8 (Raga et al. 2013). The first was Hurricane Barbara (28–30 May), which had maximum sustained winds of 65 kt (33 m s^{-1}) and a minimum central pressure of 983 hPa. Barbara made landfall in Chiapas, Mexico, on 29 May and became the easternmost storm in the historical record to make landfall in the basin. Ahead of the storm, moderate rains fell in El Salvador, resulting in flooded roads and some damaged homes. In Mexico, Barbara brought torrential rains in a 24-hour period, severely impacting small fishing villages and flooding roads leading to many resorts in Acapulco, Mexico.

Hurricane Erick had maximum sustained winds of 70 kt (36 m s^{-1}) and moved northwest and parallel to the coasts of Mexico and Baja California. Although the storm remained offshore throughout its lifecycle, extensive flooding was reported in Nayarit, Mexico, with rivers overflowing their banks and hundreds of people being rescued from the floodwaters.

Tropical Storm Ivo impacted Mexico in late August. Similar to Erick, Ivo moved northwest roughly parallel to the Mexican coastline. Maximum sustained winds for Ivo reached 40 kt (21 m s^{-1}) and the storm forced the closure of seven ports in Baja California. Rains from Ivo damaged highways and water supply lines to the city of Loreto were destroyed. While the storm quickly dissipated before making landfall, residual moisture was channeled northward into the southwestern United States, causing heavy flooding rains from San Bernardino County to Needles, California, and eventually Las Vegas, Nevada.

The strongest storm of the season was Major Hurricane Raymond, which developed on 20 October south of Acapulco, Mexico. Within 24 hours of initial development, Raymond achieved hurricane status and further strengthened until reaching peak intensity with maximum sustained winds of 140 kt (72 m s^{-1}). Though Raymond never made landfall, its close proximity to the Mexican coast led to periods of heavy rainfall near Acapulco over a 48-hour period. The flooding rains left nearly 600 residents homeless in the Mexican state of Guerrero.

4) WESTERN NORTH PACIFIC BASIN—S. J. Camargo

The TC season in the Western North Pacific (WNP) Basin for 2013 was above normal, and this takes into account most measures of TC activity.

According to the Joint Typhoon Warning Center (JTWC), there were a total of 35 TCs that were active in the basin, which is equal to the top 25th percentile of the climatological distribution. Twenty-nine became named tropical storms (the climatological median is 26, the 75th percentile is 29.5), sixteen of which became typhoons, and five evolved into super typhoons, as noted in Fig. 4.19a. The Regional Specialized Meteorological Center (RSMC), Tokyo, operated by the Japan Meteorological Agency (JMA), compiled tracks for a total of 31 TCs (in the top quartile of the JMA climatological distribution of 27), with 10 tropical storms, 8 severe tropical storms, and 13 typhoons. The climatological average numbers of TCs (1951–76) or tropical storms, super tropical storms, and typhoons (1977–2013) according to JMA are depicted in Fig. 4.19b. The 1981–2010 median IBTrACS seasonal averages for the basin are 25 tropical storms, 16.5 typhoons, and 7.5 major typhoons.

The first storm of 2013 was Tropical Storm Sonamu, which formed in January, followed by Tropical Depression 02W in February. There were no storms during March, April, or May. This lull was followed by the active month of June, when four TCs formed: Tropical Storms Yagi, Leepi, and Bebinca, and Typhoon Rumbia. In contrast, July was a quiet month, with only two storms: Tropical Storm Cimaaron and Typhoon Soulik. Eight storms were active in the WNP in August: Tropical Depression 13W; Tropical Storms Jebi, Mangkhut, Unala, and Kong-Rey; Typhoons Trami and Pewa; and Super Typhoon Utor; while Tropical Storm Unala and Severe Tropical Storm Pewa both formed in the Central North Pacific basin and moved into the Western North Pacific.

In September, six storms formed: Tropical Depression 18W, Tropical Storms Toraji and Man-Yi, Typhoons Pabuk and Wutip, and Super Typhoon Usagi. October had nine TCs active in the basin, matching the previous historical record: Tropical Depression 27W; Tropical Storm Sepat; Typhoons Fitow, Nari, Wipha, and Krosa; and Super Typhoons Danas, Francisco, and Lekima. November had three storms: Tropical Depression Podul, Tropical Storm 30W, and the very powerful Super Typhoon Haiyan (see Sidebar 4.2 for more details). Climatologically, 64% of tropical storms reach typhoon intensity; in 2013 only 55% percent reached this threshold. In contrast, climatologically 23% of typhoons attain super typhoon intensity; in 2013 the percentage was higher at 31%.

The cumulative number of named storms (Fig. 4.19c) and super typhoons were above normal, and

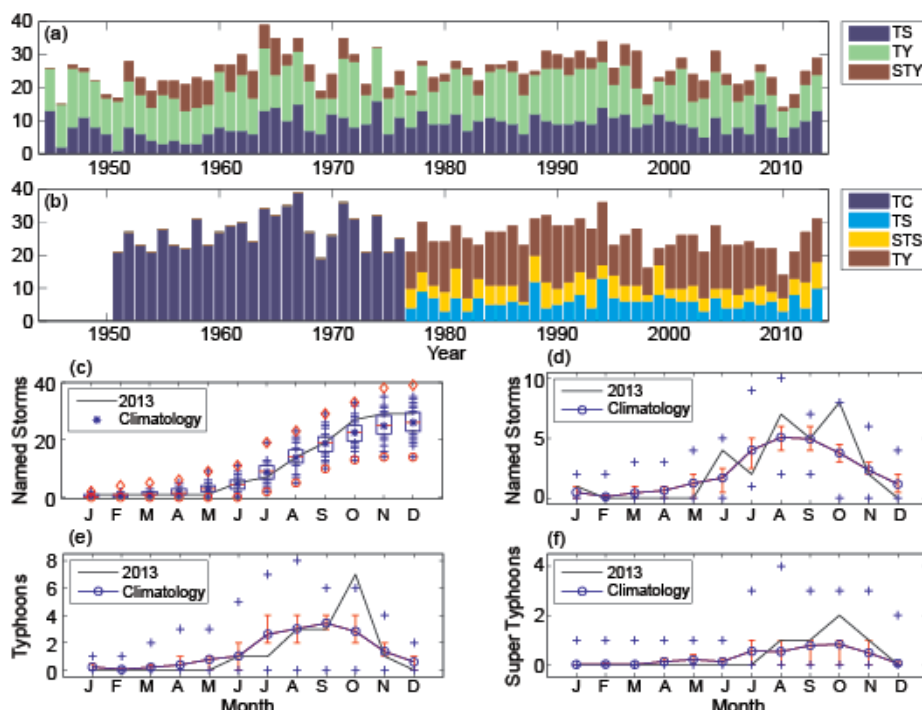


FIG. 4.19. (a) Number of tropical storms (TSs), typhoons (TYs) and super typhoons (STYs) per year in the western North Pacific (WNP) for the period 1945–2013 based on the JTWC best-track dataset. (b) Number of tropical cyclones (TCs, TS intensity or higher) from 1951 to 1976; number of TSs, severe tropical storms (STSs) and TYs from 1977 to 2013 based on the JMA best-track dataset. (c) Cumulative number of tropical cyclones with TS intensity or higher (named storms), per month in the WNP: 2013 (black line), and climatology (1971–2010) as box plots [interquartile range: box, median: red line, mean: blue asterisk, values in the top or bottom quartile: blue crosses, high (low) records in the 1945–2012 period: red diamonds (circles)]. Panels (d), (e), and (f) show the number of NSs, TYs and STYs, respectively, per month in 2013 (black line) and the climatological mean (blue line), the blue plus signs denote the maximum and minimum monthly historical records and the red error bars show the climatological interquartile range for each month (in the case of no error bars, the upper and/or lower percentiles coincide with the median. [Sources: 1945–2012 JTWC best-track dataset, 2013 JTWC preliminary operational track data for panels (a), (c), (d), (e), and (f). 1951–2013 RSMC-Tokyo, JMA best-track dataset for panel (b).]

close to the 75th percentile range of the climatological averages (29.5 tropical storms and 5 super typhoons). In contrast, the cumulative number of typhoons was equal to the mean climatological value of 16. Climatologically, June was a very active month with four TCs; the maximum number of TCs in June in the historical record was five (in 2004; see Fig. 4.19d).

The total ACE was close to the climatological median (Fig. 4.20a). The bulk of the seasonal ACE occurred in October, when four typhoons and three super typhoons were active in the basin and was the second highest in the historical record for that month, behind 1992. The only other month with an above-normal ACE value was November, largely attributed to Super Typhoon Haiyan; total ACE was in the top

quartile of the climatological distribution for that month. Individually, Super Typhoon Haiyan (3–11 November) and Super Typhoon Francisco (16–25 October) each had ACE values in the top decile per storm climatologically and contributed 13.3% and 12.6%, respectively, to the total basin ACE in 2013. Other TCs in the top quartile of the climatological and historical distributions of ACE per storm were Super Typhoons Lekima, Usagi, Soulik, and Utor, contributing a combined 57.3% of the total ACE for the season.

There were 136.5 days with TCs in 2013, below the climatological median of 157.25. There were 97.75 days with storms that reached tropical storm intensity or higher, also below the climatological median of 111.75. From those active days, 50.75 had typhoons, below the climatological median of 55.6 days. There were 21

days with major typhoons (Categories 3–5), slightly above the climatological median of 20 days. In 2013, the percentage of days with typhoons and super typhoons were 37% and 15%, near the climatological median (38%) and the 75th percentile (16%) of their climatological distributions, respectively. The median lifetime of named storms in 2013 was 6 days, below the climatological median of 8 days and close to the climatological bottom quartile (5.75 days). From the 29 TCs, 11 had a lifetime in the bottom quartile of the climatology, and only 1 in the top quartile (weak Tropical Storm 30W), which lasted 19.5 days, but reached tropical storm intensity for just a short time (and the reason it was named). Super Typhoon

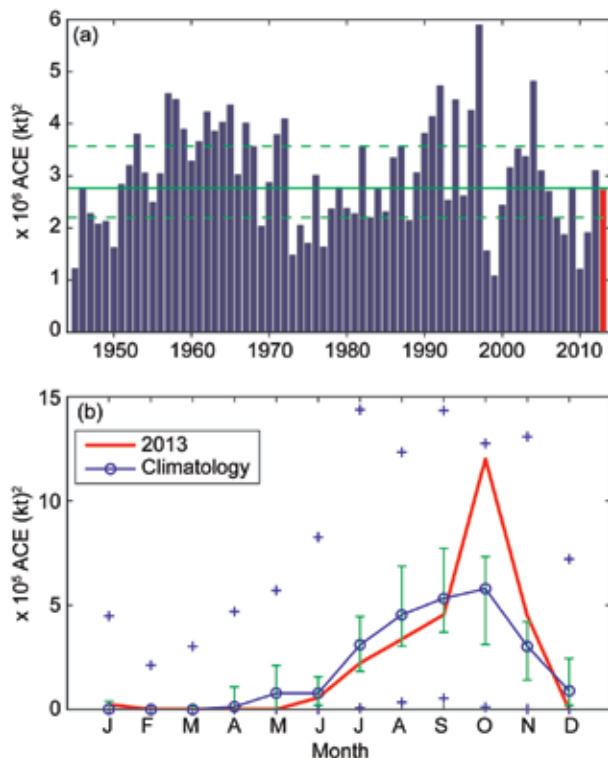


FIG.4.20. (a) Accumulated Cyclone Energy (ACE) index per year in the WNP for 1945–2013. The solid green line indicates the median for the climatology years 1971–2010, and the dashed lines show the climatological 25th and 75th percentiles. (b) ACE index per month in 2013 (red line) and the median during 1971–2010 (blue line), where the green error bars indicate the 25th and 75th percentiles. In case of no error bars, the upper and/or lower percentiles coincide with the median. The blue “+” signs denote the maximum and minimum values during the period 1945–2012. [Source: 1945–2012 JTWC best-track dataset, 2013 JTWC preliminary operational track data.]

Francisco and Typhoon Pewa were the second most long-lived storms of the season, each lasting 10 days.

The mean genesis location in 2013 was 15.2°N, 137.1°E, which was shifted northwestward of the climatological mean genesis position (13.1°N, 142.8°E). The mean track position (20.5°N, 128.6°E) was also shifted northwestward of the mean climatological track position (19.1°N, 133.7°E). This northwestward shift is typical of La Niña years; however, in 2013 ENSO-neutral conditions were present throughout the year. Nineteen TCs made landfall in 2013, above the 1951–2010 climatological 75th percentile of 18 (median is 15). Eight systems made landfall as a tropical depression (median is three); five storms made landfall as a tropical storm (median is six); five made landfall as a typhoon with Category 1–2 (median is

four); and one, Super Typhoon Haiyan, as an intense major TC (mean³ is 0.7).

Figure 4.21 shows environmental conditions associated with the TC activity in 2013. The SST anomalies in the July–October period (Fig. 4.21a) were small in the basin, with exception of a positive anomaly near Japan. The monsoon trough zonal winds (Fig. 4.21b) maximum extension was just east of the Philippines and, together with the 600-hPa relative humidity positive anomalies in the western part of the basin (Fig. 4.21c), can explain the westward shift in the genesis location in the basin. Not surprisingly, the genesis potential index (GPI; Emanuel and Nolan 2004; Camargo et al. 2007) also had positive anomalies in the western part of the basin, especially near the Philippines and the South China Sea. With respect to Super Typhoon Haiyan, more details are presented in Sidebar 4.2.

5) NORTH INDIAN OCEAN—M. C. Kruk and K. L. Gleason

The North Indian Ocean (NIO) TC season typically extends from April to December, with two peaks in activity, during May–June and again in November when the monsoon trough is positioned over tropical waters in the basin. TCs in the NIO basin normally develop over the Arabian Sea and Bay of Bengal between 8° and 15°N. These systems are usually short-lived and relatively weak, and often quickly move into the Indian subcontinent.

According to the JTWC, the 2013 TC season produced six tropical storms, three cyclones, and one major cyclone (Fig. 4.22a). The 1981–2010 IBTrACS seasonal averages for the basin are 3.9 tropical storms, 1.4 cyclones, and 0.6 major cyclones. The season produced its highest ACE index since 1972 with a value of $48.9 \times 10^4 \text{ kt}^2$, which is almost four times higher than the 1981–2010 mean of $12.5 \times 10^4 \text{ kt}^2$ (Fig. 4.22b). Typically, there is enhanced TC activity, especially in the Bay of Bengal, during the cool phase of ENSO (Singh et al. 2000); however, most of this season was characterized by near-neutral ENSO conditions.

The NIO season started much earlier when compared to the 2012 season (Diamond 2013), with the first storm occurring 10–16 May. Cyclone Mahasen developed in the central Bay of Bengal and began a slow westward and then northward track towards Bangladesh. The storm made landfall on 16 May near the Patuakhali district of Bangladesh, with maximum sustained winds of 50 kt (26 m s^{-1}) and

³ The mean is used for this category as the median is 0.

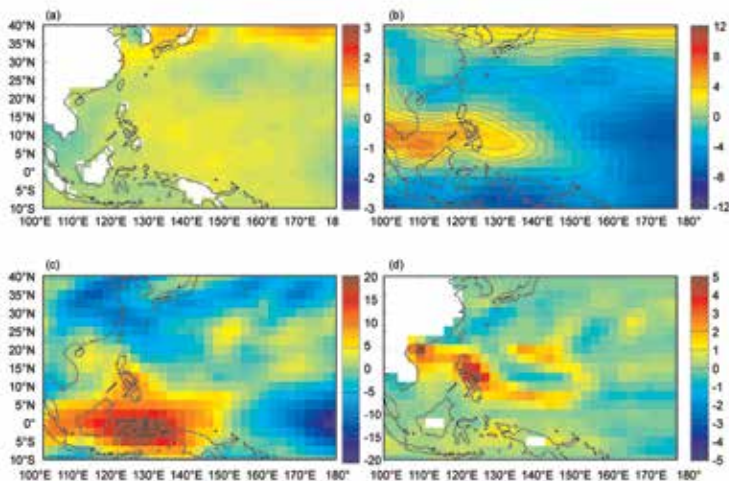


FIG. 4.21. (a) SST anomalies for Jul–Oct (JASO) 2013. (b) Zonal winds in JASO 2013 (positive contours are shown in solid lines, negative contours in dash dotted lines and the zero contour in a dotted line) (c) Relative humidity 600-hPa anomalies in JASO 2013 (d) Genesis potential index anomalies in JASO 2013. [Source: atmospheric variables: NCEP/NCAR reanalysis data (Kalnay et al. 1996); SST (Smith and Reynolds 2005)].

produced widespread destruction to coastal areas. More than 60 deaths were reported in Bangladesh and neighboring Myanmar.

The most noteworthy storm of the season was Phailin, which became a very severe cyclonic storm during 9–12 October with peak winds of 140 kt (72 m s^{-1}) and an estimated minimum central pressure of 910 hPa. Phailin made landfall with 100 kt (52 m s^{-1}) winds near Gopalpur along the Odisha coast on 12 October and became the second strongest storm ever to make landfall in India, following that of Cyclone 05B (the Odisha super cyclone) in 1999. Phailin is noted for its rapid intensification over the Bay of Bengal, increasing from 65 kt (33 m s^{-1}) sustained winds to over 125 kt (64 m s^{-1}) in just a 12-hour period. The cyclone maintained at least 100 kt (52 m s^{-1}) winds for 63 consecutive hours, helping propel the storm's ACE value to $17.5125 \times 10^4 \text{ kt}^2$, or about 35% of the entire season's ACE total.

Heavy rainfall, averaging 250–350 mm, led to flooding and landslides in the interior areas of Odisha and Andhra Pradesh, while storm surge flooding was prevalent along the Odisha coastline. It was also estimated that over 250 000 homes were partially or fully destroyed and more than 600 000 hectares of agriculture were lost. Due to vastly improved early warning systems and preparedness, the death toll from Phailin was estimated to be 39. This contrasts with the nearly 10 000 people who were killed during the 1999 Odisha super cyclone.

Cyclones Helen (19–23 November) and Lehar (19–28 November) both impacted southern India. Helen formed in the Bay of Bengal near the Andaman Islands on 17 November and slowly gathered strength before reaching TC status on the 19th. The storm had maximum sustained winds of 60 kt (31 m s^{-1}) before interacting with the Indian subcontinent and weakening, making landfall just south of Machilipatnam, Andhra Pradesh.

Cyclone Lehar was the second most intense storm of the 2013 NIO season, with peak maximum sustained winds of 75 kt (39 m s^{-1}). Lehar developed over the Malay Peninsula and intensified as it moved into the warmer waters of the Andaman Sea and eventually the Bay of Bengal. It continued on a slow west-northwest track until landfall in Andhra Pradesh and Odisha on 28 November.

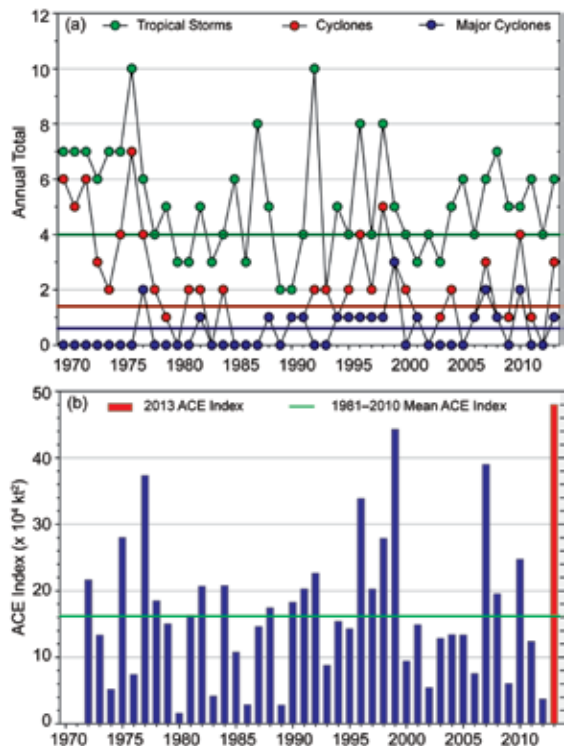


FIG. 4.22. Annual TC statistics for the NIO for 1970–2013: (a) number of named storms, cyclones, and major cyclones and (b) the estimated annual ACE Index (in $\text{kt}^2 \times 10^4$) for all TCs during which they were at least tropical storm strength or greater intensity (Bell et al. 2000). The 1981–2010 base period means are included in both (a) and (b).

6) SOUTH INDIAN OCEAN—K. L. Gleason and M. C. Kruk

The South Indian Ocean (SIO) Basin extends south of the equator from the African coastline to 105°E⁴, with most cyclones developing south of 10°S. The SIO TC season extends from July to June encompassing equal portions of two calendar years (the 2013 season is comprised of storms from July to December 2012 and from January to June 2013). The peak activity typically occurs during December–April when the ITCZ is located in the Southern Hemisphere and migrating toward the equator. Historically, the vast majority of landfalling cyclones in the SIO impact Madagascar, Mozambique, and the Mascarene Islands, including Mauritius and La Réunion.

The historical SIO TC data is probably the least reliable of all the TC basins (Atkinson 1971), primarily due to a lack of historical record keeping by individual countries and no consistent, centralized monitoring agency; however, the historical dataset for the region has been updated (Knapp et al. 2010). The historical data are noticeably deficient before reliable satellite data were operationally implemented in the region beginning about 1983. The RSMC on La Réunion now serves as the official monitoring agency for TC activity within the basin (WMO 2012).

The 2012/13 SIO storm season was near average with ten tropical storms, seven cyclones, and one major cyclone (Fig. 4.23a). The 1981–2010 IBTrACS seasonal median averages are eight tropical storms, four cyclones, and one major cyclone. The season is also reflected in the 2012/13 ACE index of 89.9×10^4 kt², which was near the 1981–2010 average of 91.5×10^4 kt² (Fig. 4.23b). This is the first year since 2008 with a near-average ACE value for the SIO; as noted in Fig 4.23b, the ACE values have been below to well below normal for that past few years.

Of note, Cyclone Anais developed in mid-October 2012 near the Chagos Islands and strengthened into a Category 3 storm, the strongest storm on record so early in the season (equivalent to a major hurricane in the Atlantic during April)⁵. The most intense storm of the season, Cyclone Felleng, attained Category 4 strength with maximum sustained winds of 89 kt (46 m s^{-1}) in late January 2013. Although it never made

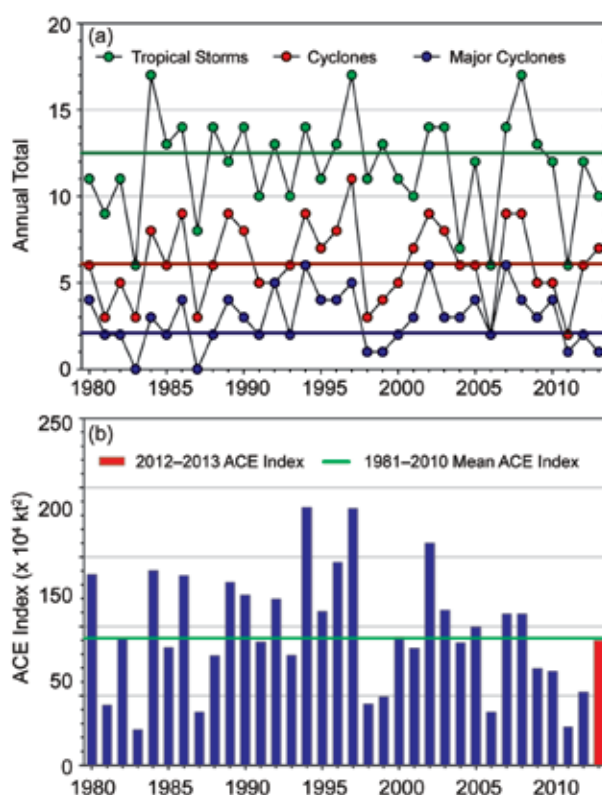


FIG. 4.23. Annual TC statistics for the SIO for 1980–2013: (a) number of tropical storms, cyclones, and major cyclones and (b) the estimated annual ACE Index (in $\text{kt}^2 \times 10^4$) for all TCs during which they were at least tropical storm or greater intensities (Bell et al. 2000). The 1981–2010 base period means are included in both (a) and (b). Note that the ACE Index is estimated due to a lack of consistent 6-h-sustained winds for each storm.

landfall, Felleng impacted both Réunion and Madagascar with heavy winds and rainfall. In La Plaine des Cafres, Réunion, 512 mm of rain fell during a 24-hour period.

Cyclone Haruna was the only TC to make landfall during the season. Resulting from a break in the subtropical ridge, Haruna vacillated over the Mozambique Channel for a week, bringing copious rainfall to the western coast of Madagascar. Peak sustained winds were measured at 81 kt (42 m s^{-1}) while Haruna remained over the Mozambique Channel. Haruna made landfall in southwestern Madagascar near Manombo as a Category 2 cyclone on 22 February with wind gusts of up to 91 kt (47 m s^{-1}). Landfalling tropical cyclones in this region of Madagascar are unusual. Twenty-six fatalities were reported and thousands were left homeless.

⁴ In order to generate consistent basin statistics, the SIO basin boundary overlaps with the Australian Bureau of Meteorology's operational warning area from 90° to 105°E.

⁵ The Saffir–Simpson scale is used as the standard in this report for identifying the intensity of TCs in the South Indian Ocean Basin.

7) AUSTRALIAN REGION BASIN—B. C. Trewin

(i) Seasonal activity

The 2012/13 TC season was near normal in the broader Australian basin (areas south of the equator and between 90° and 160°E, which includes Australian, Papua New Guinea, and Indonesian areas of responsibility). The season produced 10 named storms, near the 1983/84–2010/11 average (coincident with comprehensive satellite coverage of the region) of 10.8, and consistent with ENSO-neutral conditions. The 1981–2010 IBTrACS seasonal averages for the basin are 9.9 named storms, 7.5 TCs, and 4.0 major TCs, which compares with the 2012/13 counts of 10, 5, and 2, respectively. TC categories in this basin are based on the Australian TC intensity scale (<http://www.bom.gov.au/cyclone/about/intensity.shtml>).

There were five named storms in the eastern sector of the Australian region during 2012/13 (two of which reached their peak intensity after moving into the southwest Pacific region), none in the northern sector, and five in the western sector. Three systems made landfall in Australia as TCs: two in Western Australia and one in Queensland.

(ii) Landfalling and other significant TCs

The most significant storm of the season in the Australian region was Tropical Cyclone Rusty. Rusty reached TC intensity on 24 February near 17°S, 118°E, and then tracked generally southwards towards the Pilbara coast of Western Australia. It reached Category 4 intensity early on 27 February, with maximum sustained winds of 90 kt (46 m s⁻¹), and weakened slightly before making landfall as a Category 3 system later that day near Pardoo Station, about 150 km east of Port Hedland. The slow movement of the cyclone resulted in an extended period of high winds and heavy rain, with gale-force winds continuing at Port Hedland for 39 consecutive hours, an unprecedented event. Rain from the remnant system extended south to Kalgoorlie and beyond; at Pardoo, 520 mm was recorded over 26–28 February. Only minor wind damage was reported from Rusty but flooding was widespread, and there was considerable disruption to the resources industry, with the port at Port Hedland closed for 86 hours.

Narelle was slightly more intense than Rusty [Category 4, maximum sustained winds 100 kt (54 m s⁻¹)]. It reached TC intensity on 8 January, well off the western Australian coast, and moved southwest roughly parallel with the coast, reaching its peak intensity on 11 January. The following day Narelle made its closest approach to the coast, passing approximately 330 km

northwest of Exmouth, before weakening steadily and falling below cyclone intensity on 15 January west of Geraldton. While Narelle did not make landfall, it disrupted shipping and offshore oil and gas operations, and its precursor low caused damaging floods in parts of Indonesia.

TC Oswald formed from a low that had been meandering in the Gulf of Carpentaria from 17 January. It reached minimal Category 1 intensity (35 kt or 18 m s⁻¹) and was named as it moved towards the east coast of the Gulf on 21 January, making landfall north of Kowanyama. The remnant tropical low remained intact and tracked southeast through inland eastern Australia, generally on a track parallel with and about 100–200 km inland from the coast, eventually emerging over water south of Sydney on 30 January. Oswald was responsible for substantial flooding over many coastal regions of Queensland and New South Wales. Among the most significantly affected regions was the Burnett River catchment in Queensland; the 1-day catchment average rainfall for 27 January of 206.8 mm exceeded the previous record by nearly 70%. The river reached a record height at Bundaberg, where extensive flooding occurred. Record flood heights also occurred on the Clarence River at Grafton, in northern New South Wales, but levees limited damage there. The Brisbane River catchment, which received similar rainfalls to those experienced in the 2011 floods, was spared similarly severe flooding because of dry antecedent conditions, although there was destructive flooding in some southern parts of the catchment, where the 24-hour rainfall total reached 744 mm at Upper Springbrook in the Gold Coast hinterland, and 709 mm at Mount Castle on the escarpment northeast of Warwick. A number of tornadoes were also reported during the event. Six deaths were attributed to Oswald and its remnant low, and reported damage was in excess of \$2 billion US dollars.

The third landfall for the season was Peta, which became a minimal Category 1 cyclone (35 kt or 18 m s⁻¹) on 23 January off the coast between Broome and Port Hedland. The storm turned southwards and made landfall that day at Point Samson, near Karratha. Shipping was disrupted and there was widespread flooding. Hooley and Wittenoom, in the inland Pilbara, recorded 377 and 350 mm of rain, respectively, during 24–25 January.

TCs Sandra and Freda were two eastern region cyclones which both peaked as Category 4 systems outside the Australian region and are described in more detail in section 4d8.

8) SOUTHWEST PACIFIC BASIN—A. M. Lorrey, N. C. Fauchereau, P. R. Chappell, S. Ready, and H. J. Diamond

(i) Seasonal activity

Tropical cyclone activity began in December 2012 and extended until the end of April, with Queensland, Australia, and Samoa experiencing significant impacts and loss of life during the course of the season. Storm track data for November 2012–April 2013 period was gathered from the Fiji Meteorological Service, Australian Bureau of Meteorology, and New Zealand MetService. Following the climatological definition put forward by Diamond et al. (2012), the Southwest Pacific Basin (135°E–120°W) had eight tropical cyclones (Fig. 4.24), including four severe tropical cyclones⁶.

The 1981–2010 South Pacific Enhanced Archive of Tropical Cyclones (SPEARTC) seasonal averages indicates 10.4 tropical cyclones and 4.3 major tropical cyclones usually occur in the basin each year. The ratio of severe TCs relative to the total number of named TCs was 50%, and significant impacts to infrastructure and loss of human life occurred in the Cook Islands even as a result of a lower-order tropical storm. Six deaths and >\$2.5 billion US dollars in damage was caused by Category 1 Tropical Cyclone

Oswald in northeast Australia, making it the most damaging storm to hit Queensland since 1999. Severe Tropical Cyclone Evan caused four deaths (with another ten missing and presumed dead) and damage in excess of \$160 million US dollars in Samoa, and there were two fatalities in New Caledonia associated with Severe Tropical Cyclone Freda.

(ii) Landfalling and other significant TCs

The first TC of the season, Evan, developed as a tropical depression within the South Pacific convergence zone (SPCZ) northeast of Fiji on 9 December. TC Evan strengthened to Category 2 status and made landfall in Samoa with maximum sustained winds in excess of 59 kt (30 m s⁻¹) and gusts up to 94 kt (48 m s⁻¹). The storm then reversed course, making a northwest loop around Samoa before turning southwest and accelerating toward Fiji. On 17 December, Evan reached Fiji as a Category 4 storm (mean central pressure of 943 hPa) and affected those islands with maximum sustained winds of up to 124 kt (64 m s⁻¹). The system turned south and began to weaken on 19 December, with the post-tropical remnants of the storm bringing heavy rain and strong winds to northern New Zealand during 21–22 December.

TC Freda spawned north of Efate, Vanuatu, and began moving westward while intensifying and becoming a Category 1 storm on 28 December as it passed south of the Solomon Islands, impacting Makira, Rennell, and Bellona Islands with strong winds, rainfall, and storm wave action. Freda turned south and peaked at Category 4 status on 30 December, with maximum sustained winds of 100 kt (51 m s⁻¹), as reported by RSMC Nadi (in Fiji). The storm weakened to a Category 1 storm before recurving southeast and clipping the northern tip of New Caledonia's Grande Terre Island followed by the Loyalty Islands on 2 January. Two people drowned in New Caledonia and more than 3000 lost power. The system dissipated on 4 January south of Fiji.

On 14 January, a tropical disturbance developed to the southeast of Guadalcanal, intensified into TC Garry while north of Wallis and Futuna, and rapidly

⁶ This basin also utilizes the Australian TC intensity scale.

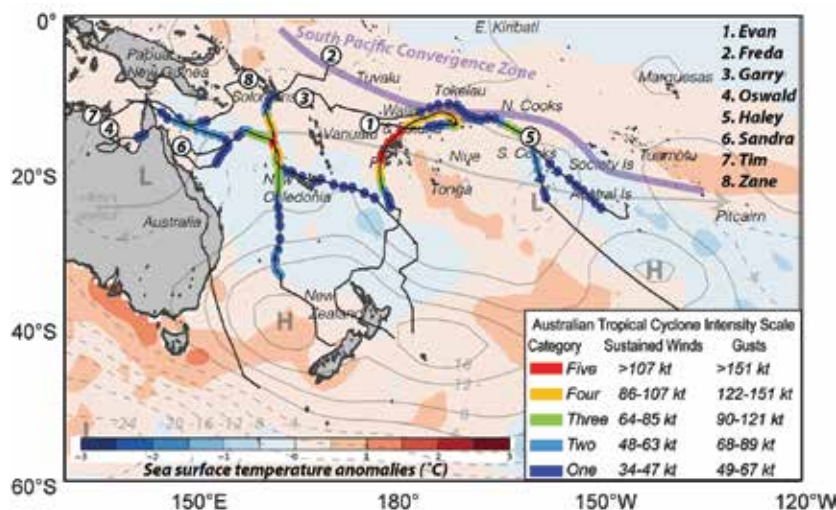


FIG. 4.24. TCs in the Southwest Pacific Basin. Solid black lines indicate each storm track, while the number for each storm (noted in chronologic sequence of occurrence in the upper right corner) indicates TC genesis location. SST anomalies (°C), 4 m s⁻¹ steering wind, surface pressure anomalies (geopotential at 1000-hPa), and the location of the SPCZ (purple line) are shown for reference. Omega (used to define the core location of the SPCZ) and the steering wind information are shown for the 500-hPa geopotential height. SST anomalies are plotted relative to the austral warm season (Nov–Apr) 1981–2010 climatology. Geopotential height contours are in meters.

traveled east towards the waters north of Samoa. TC Garry increased to a Category 2 strength system on 22 January with a minimum central pressure of 984 hPa and tropical storm force winds extending 50 nautical miles from the storm eye and sustained at 45 kt (23 m s⁻¹) with wind gusts of up to 50 kt (26 m s⁻¹). Garry peaked as a Severe Category 3 storm north of Suvarrow and Palmerston Island in the Northern Cook Islands, with average wind speeds estimated at 80 kt (41 m s⁻¹) and gusts up to 110 kt (57 m s⁻¹).

In January, a Category 1 TC, Oswald, made land-fall on the Cape York Peninsula on 21 January with winds of 35 kt (18 m s⁻¹). The storm traversed the peninsula and turned due south, traveling almost the entire length of Queensland over land as a deteriorating system. Significant impacts from waves and winds in Cairns included downed power lines and damage to coastal communities, with many extreme rainfall records broken that led to flooding and road closures. Total damages exceeded \$2.5 billion US dollars and six people died.

The final severe TC during the season formed on 7 March in the Queensland region and was named Sandra the next day as it rapidly intensified in the Coral Sea from a Category 1 to Category 2 tropical cyclone. Convection strengthened over TC Sandra's center as it was located northwest of Noumea, New Caledonia, while it moved eastward into RSMC Nadi's area of responsibility and further intensified into a Severe Category 3 system (minimum central pressure estimated at 968 hPa). Upon reaching Category 4 status on 9 March over the eastern Coral Sea, wave action and maximum sustained winds of 76 kt (39 m s⁻¹) with gusts in excess of 108 kt (56 m s⁻¹) impacted the Solomon Islands. Vanuatu received in excess of 380 mm of rainfall at some locations. The storm turned southeast, then due south, tracking along a trajectory to the west of New Caledonia when it peaked on 11 March with maximum sustained wind speeds of 105 kt (54 m s⁻¹). On 13 March, TC Sandra then passed within 220 km of Lord Howe Island in the North Tasman Sea as a Category 1 storm on 14 March, bringing destructive wind gusts of 81 kt (42 m s⁻¹) that downed trees and littered roads with debris along with heavy ocean swells that brought rough surf and rip currents to Australia's east coast. Remnants of the storm brought severe thunderstorms, tornadoes, and heavy rainfall to the Taranaki region of New Zealand's North Island.

e. *Tropical cyclone heat potential*—G. J. Goni, J. A. Knaff, and I-I Lin

This section summarizes the previously described TC basins from the standpoint of tropical cyclone heat potential (TCHP), by focusing on upper ocean temperature conditions during the season with respect to average values. The TCHP (Goni and Trinanes 2003), defined as the excess heat content above 26°C in the water column contained between the sea surface and the depth of the 26°C isotherm, has been linked to TC intensity changes (Shay et al. 2000; Goni and Trinanes 2003; and I-I Lin et al. 2008, 2009). In addition, the magnitude of the in situ TCHP has also been identified as impacting maximum potential intensity (MPI) through modulating the during-TC air-sea coupling flux supply (Mainelli et al. 2008; Lin et al. 2013). In general, fields of TCHP show high spatial and temporal variability associated with oceanic mesoscale features, interannual variability, or long-term decadal variability that can be detected with satellite altimetry (Goni et al. 1996; I-I Lin et al. 2008; Goni et al. 2009; Pun et al. 2014).

To examine the TCHP interannual variability, anomalies (departures from the 1993–2012 mean values) are computed during the months of TC activity in each hemisphere: June–November in the Northern Hemisphere and November–April in the Southern Hemisphere. In general, these anomalies show large variability within and among the TC basins.

In most of the ocean basins, the number of tropical cyclones remained similar to last year, except for the tropical Atlantic. Most of the basins continue to exhibit positive TCHP anomalies, except for the Arabian Sea and large areas of the South Pacific Basin (Fig. 4.25). The North Atlantic Basin continued exhibiting positive anomaly values of TCHP as previous years. However, there was only one hurricane in the Gulf of Mexico and one in the tropical North Atlantic, compared with 12 hurricanes in this region during the 2012 season. The Gulf of Mexico (part of the North Atlantic Basin) continued exhibiting positive anomalies except for a region susceptible to the spatial variability of the Loop Current, which had negative anomalies. The WNP Basin usually exhibits anomalies related to ENSO variability, and has been undergoing a long-term decadal subsurface warming associated with the La Niña-like conditions over the last decade (Kosaka and Xie 2013; England et al. 2014). The TCHP over the west Pacific MDR (4°–19°N, 122°E–180°) has been observed to increase considerably as well (Pun et al. 2013; Goni et al. 2013). During 2013, this warming continued in the western

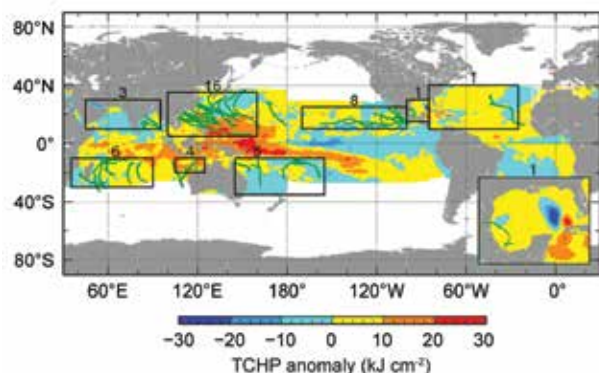


FIG. 4.25. Global anomalies of TCHP corresponding to 2013 computed as described in the text. The boxes indicate the seven regions where TCs occur: from left to right, SIO, NIO, NWP, Southeast Indian, Southwest Pacific, ENP, and North Atlantic (shown as Gulf of Mexico and tropical Atlantic separately). The green lines indicate the trajectories of all tropical cyclones reaching at least Category 1 (1-minute average wind ≥ 64 kts) and above during Nov 2012–Apr 2013 in the Southern Hemisphere and Jun–Nov 2013 in the Northern Hemisphere. The numbers above each box correspond to the number of Category 1 and above cyclones that travel within each box. The Gulf of Mexico conditions during Jun–Nov 2013 are shown in the insert in the lower right corner.

North Pacific and TCHP is currently at the highest level in 20 years. The TCHP fields in the west Pacific MDR since 1993, when altimetry became available, have increased by an average of 15%.

For each basin, the differences in the TCHP values between the most recent cyclone season and the previous season (Fig. 4.26) follow the same overall pattern as the differences between the 2012 and 2011 seasons (Goni et al. 2013). Some notable differences occurred in the NWP; west of Madagascar in the SIO; the NIO in the Bay of Bengal; and the northern tropical and subtropical areas of the North Atlantic, where TCHP values increased with respect to the previous season. The largest changes were in the South Pacific where warm anomalies are depicted in a large region toward the central equatorial Pacific while negative anomalies developed in the subtropics off the eastern coast of Australia.

During the 2013 season, the basins exhibited the following TCHP anomalies:

- As described in section 4d4, four TCs attained Category 5 super typhoon intensity. The most notable was Haiyan, which intensified over the WNP region from a Category 1 to a Category 5 storm associated with significant subsurface warming over a region of high TCHP values that ranged from 100–125 kJ cm⁻² (Fig. 4.27b).

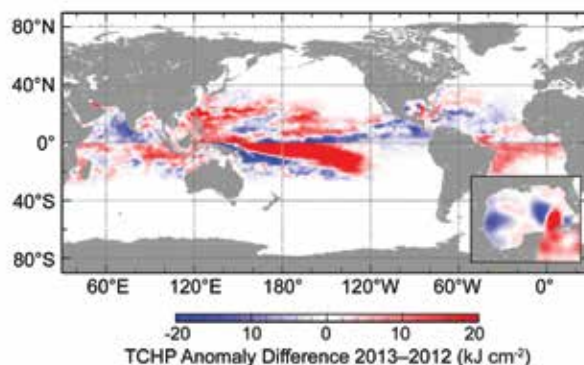


FIG. 4.26. Differences between the TCHP fields in 2013 and 2012.

In the WNP, as confirmed by two decades of the TAO/Triton mooring and satellite observations, the TCHP increased by about 10%, as compared to the early 90s (Pun et al. 2013). Haiyan's fast translation speed (7–11 m s⁻¹) during intensification minimized the cooling effect. As Haiyan continued traveling over this favorable TCHP region with subsurface warmth for another 36 hours, its sustained winds reached the highest wind speed ever assigned to a TC by the JTWC with a value of 170 kt (85 m s⁻¹). Typhoon Usagi intensified over the same region, and within 24 hours, it also rapidly intensified into a Category 5 system. The pre-typhoon TCHP values ranged from 110–125 kJ cm⁻², comparable to Haiyan (Fig. 4.27a).

- In the NIO Basin, TC Phailin (Fig. 4.27c) was the second strongest TC to make landfall in India on record. On 10 October, Phailin became a Category 1 tropical cyclone in the Bay of Bengal and one day later rapidly intensified to a Category 5 TC, with maximum sustained winds of 160 kt (82 m s⁻¹). This intensification coincided with its path traveling over warm waters with TCHP values slightly above 50 kJ cm⁻². The intensification of this cyclone produced a cooling of the surface waters of approximately 3°C.
- In the SIO Basin, TC Felleng formed in January 2013, reaching maximum intensity of 115 kt (59 m s⁻¹) at approximately 16.2°S on 30 January at 1200 UTC. The TCHP under this TC track only reached 50 kJ cm⁻² at the time of its maximum intensity (Fig. 4.27d); however, the storm developed a well-defined eye, with a deep, intense ring of convection forming in the eyewall (<http://weather.noaa.gov/pub/data/raw/wt/wtio30.fmee.txt>). The associated cooling of 3°C and 25 kJ cm⁻² in SST and TCHP, respectively, are typical values for intense TCs.

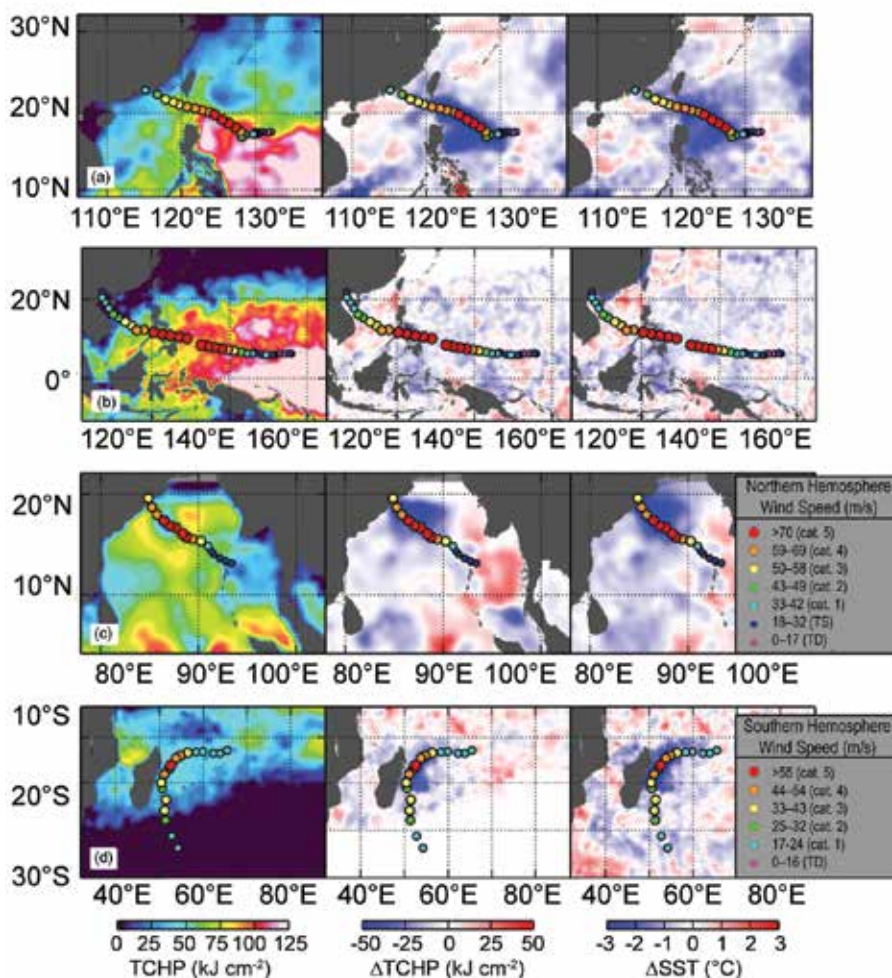


FIG. 4.27. (Left) TCHP and surface cooling given by the difference between post and pre storm values of (center) tropical cyclone heat potential and (right) sea surface temperature for tropical cyclones (a) Usagi, (b) Haiyan, (c) Phailin, and (d) Fellingeng. The TCHP values correspond to two days before each cyclone reaches its maximum intensity value.

f. Global monsoon summary—B. Wang

Global monsoon (GM) is the dominant mode of annual variation of the tropical-subtropical precipitation and circulation (Wang and Ding 2008), and thus a defining feature of seasonality and a major mode of variability of the Earth's climate system. Figure 4.28 summarizes the monsoon rainfall anomalies for the period November 2012–October 2013, which is a global monsoon year that includes both the SH summer monsoon (SHSM) from November 2012 to April 2013 and the NH summer monsoon (NHSM) from May to October 2013.

The global land monsoon precipitation is strongly influenced by the status of ENSO, especially the land areas of Asia, Australia, northern Africa, and Central America (Wang et al. 2012). From November 2012 to October 2013, the equatorial Pacific SSTs were

near normal except for a moderate cooling in the far eastern Pacific. Given the ENSO-neutral status, no coordinated monsoon rainfall anomalies were expected on a global scale, and as such the global monsoon anomalies would be expected to be near average overall. This was indeed the case for 2013, as shown in Fig. 4.28. Significant monsoon rainfall anomalies, however, did occur on local and regional scales. The SHSM rainfall over land areas tended to be moderately below normal with deficient rainfall over northeast Australia and Madagascar. The NHSM rainfall over land shows a mixed pattern of regional anomalies: above-normal rainfall occurred over northern India and southwest Mexico while deficient rainfall occurred in the East Asian subtropics and Nigeria–Cameroon.

Figure 4.29 shows the time series of the monsoon precipitation and low-level circulation indices. Note that the precipitation indices represent the total amount of precipitation over both land and ocean. The definitions of circulation indices for each monsoon region are shown in Table 4.1 (Yim et al. 2013). In 2013, the majority of summer monsoon systems, including western North Pacific (WNP), North American (NA), northern African (NAF), southern African (SAF), and Australian (AUS), had normal seasonal mean strength with an average precipitation and circulation index value <0.5 standard deviation. The precipitation and circulation indices together represent the strength of each regional monsoon system. The Indian (I) summer monsoon in 2013 was strong (the precipitation index was $+0.8$ standard deviation and the circulation index was $+2.5$ standard deviation). On the other hand, the East Asian (EA) summer monsoon and South American (SA) summer

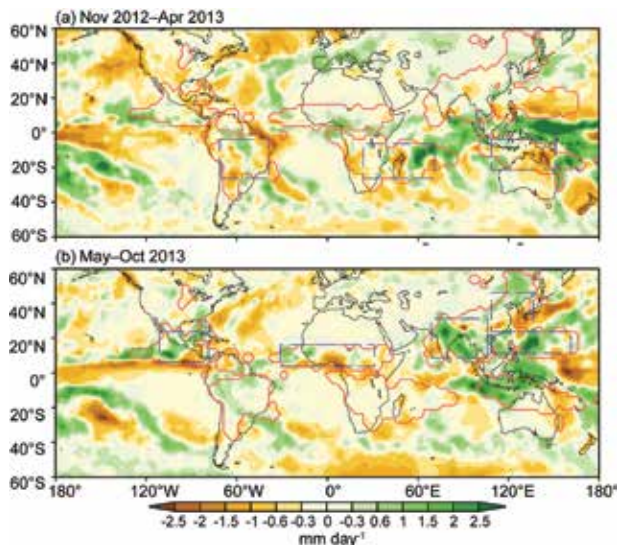


FIG. 4.28. Precipitation anomalies (mm day^{-1}) averaged for (a) Nov 2012–Apr 2013 and (b) May–Oct 2013. The red lines outline the global monsoon precipitation domain that is defined by (a) the annual range (local summer minus winter) precipitation exceeding 300 mm and (b) the summer mean precipitation exceeding 55% of the total annual precipitation amount (Wang and Ding 2008). Here the local summer denotes May–Sep for the NH and Nov–Mar for the SH. The precipitation indices for each regional monsoon are defined by the areal mean precipitation in the corresponding rectangular regions (dashed blue), which are highly correlated with the precipitation averaged over the corresponding real regional monsoon domains. The rainfall data are from the Global Precipitation Climatology Project analysis (Huffman et al. 2009).

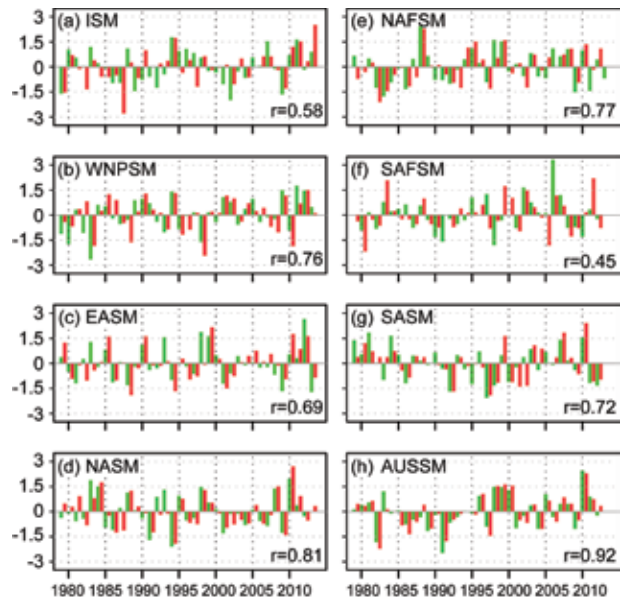


FIG. 4.29. Normalized summer mean precipitation (green) and circulation (red) indices in each of eight regional monsoons. The indices are normalized by their corresponding standard deviation. The numbers shown in the corner of each panel denote the correlation coefficient between seasonal mean precipitation and circulation indices.

monsoon systems were below normal by about one standard deviation. The compensation between the Indian and East Asian summer monsoon made the total NHSM near normal. The total strength of the SHSM was also slightly negative but remained in the

Table 4.1. Definition of regional summer monsoon circulation indices and their correlation coefficients (CCs) with the corresponding regional summer monsoon precipitation indices for the period 1979–2013. All circulation indices are 850-hPa vorticity indices except northern African (NAF) and East Asian (EA). The correlation coefficients were computed using monthly time series [June–September in NH and December–March in SH]. The bolded numbers represent significance at 99% confidence level.

Region	Definition of Vorticity Circulation Index	CC
I	U850 (5° – 15° N, 40° – 80° E) minus U850 (25° – 35° N, 70° – 90° E)	0.76
WNP	U850 (5° – 15° N, 100° – 130° E) minus U850 (20° – 35° N, 110° – 140° E)	0.82
EA	V850 (20° – 40° N, 120° – 140° E)	0.70
NA	U850 (5° – 15° N, 130° – 100° W) minus U850 (20° – 30° N, 110° – 80° W)	0.82
NAF	U850 (0° – 15° N, 60° – 10° W)	0.74
SA	U850 (5° – 20° S, 70° – 40° W) minus U850 (20° – 35° S, 70° – 40° W)	0.81
SAF	U850 (5° – 15° S, 20° – 50° E) minus U850 (20° – 30° S, 30° – 55° E)	0.70
AUS	U850 (0° – 15° S, 90° – 130° E) minus U850 (20° – 30° S, 100° – 140° E)	0.90

near-normal range. Note that these results are for the summer mean monsoon strength. Over the Indian and WNP summer monsoon regions, there were large month-to-month fluctuations due to intraseasonal oscillation. The Indian monsoon was strong in June and July, but became weak in August. The WNP monsoon became extremely strong in September (not shown), and remained that way through early November. The other regions had moderate month-to-month variation.

g. Intertropical convergence zones

1) PACIFIC—A. B. Mullan

The Pacific intertropical convergence zone (ITCZ) lies approximately parallel to the equator with a slight northeasterly tilt, and varies in position from around 5°–7°N during February–May to 7°–10°N in August–November. The South Pacific convergence zone (SPCZ) extends diagonally from around Solomon Islands (10°S, 160°E) to near 30°S, 140°W, and is most active during November–April. In the far western Pacific, these two convergence bands merge into the Australian and East Asian monsoon troughs, which are most active in the summer seasons of their respective hemispheres: December–March in the South Pacific (northern Australia) and June–September in the western North Pacific (Federated States of Micronesia, Republic of Marshall Islands, and other U.S.-affiliated Pacific islands).

The positions of the Pacific convergence zones are strongly influenced by the status of ENSO, and because of the strong meridional rainfall gradients in the convergence zones, so is rainfall on many Pacific islands. In general, both the ITCZ and SPCZ are closer to the equator in El Niño seasons. During 2013, ENSO-neutral conditions generally prevailed; however, some La Niña characteristics were present during the year, with below-average sea surface temperatures in the eastern equatorial Pacific for January–August, and slightly enhanced low-level easterly trade winds in the western half of the Pacific basin for much of the first half of 2013.

NASA's ENSO Precipitation Index (Curtis and Adler 2000; http://trmm.gsfc.nasa.gov/trmm_rain/Events/thirty_day.html), which quantifies the rainfall changes in the Indonesian and central Pacific regions from the TRMM rainfall imagery, was below -1.0 (La Niña-like rainfall pattern) for most of the April–August period.

Figure 4.30 summarizes the convergence zone behavior for 2013 and allows comparison of the 2013 seasonal variation against the 1998–2012 climatology. Rainfall transects over 20°N to 30°S are presented for each quarter of the year, averaged across successive 30° longitude bands, starting in the western Pacific at 120°–150°E.

For January–September 2013 (Figs. 4.30a–c), the ITCZ exhibited a more skewed orientation than usual, being slightly closer to the equator west of the dateline, but farther north in the 150°–120°W sector. West of the dateline (150°E–180° sector), the equatorward displacement of the ITCZ produced significant drought conditions in many western Pacific U.S. islands (<http://www.prh.noaa.gov/peac/>), including Yap (8°N), Guam (13.5°N), and Kwajalein (9°N). The large anomalously dry region in the western Pacific around 10°N and corresponding wetter conditions at similar latitudes east of 150°W are evident in the 2013 annual-average anomaly rainfall field (Fig. 4.31). The enhanced dryness along the equator near the dateline, a feature often occurring in La Niña years, is also evident in Figs. 4.30 and 4.31.

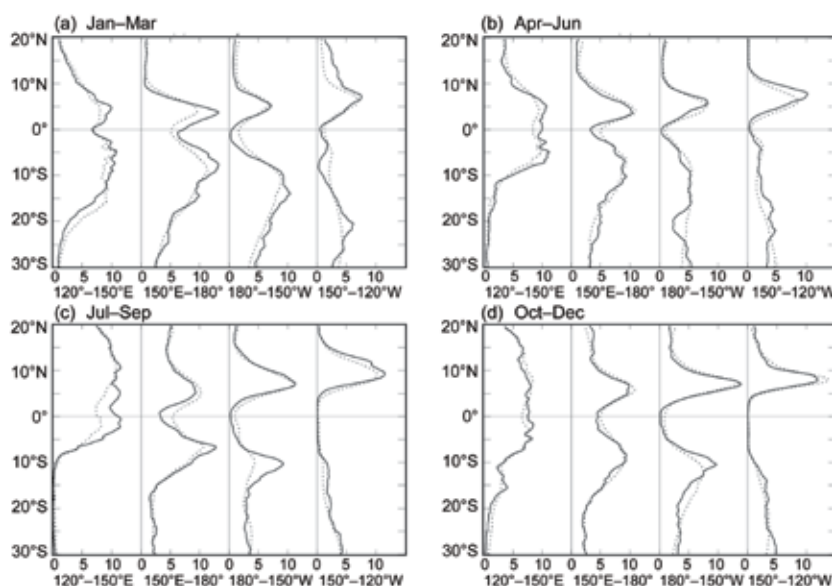


FIG 4.30. Rainfall rate (mm day⁻¹) from TRMM analysis (3B43 version 7) for the four quarters of 2013 (a–d). The separate panels within each quarter show the 2013 rainfall cross-section between 20°N and 30°S (solid line) and the 1998–2012 climatology (dotted line) for four 30° sectors from 120°–150°E to 150°–120°W.

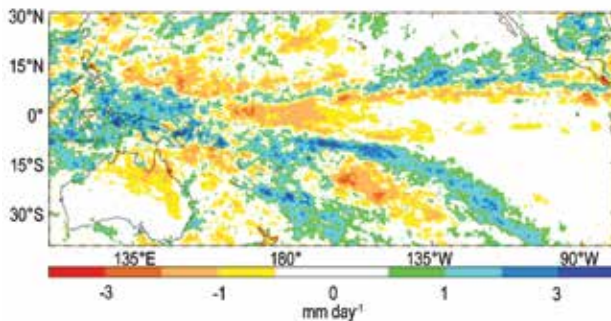


FIG 4.31. TRMM-3B43 annual average precipitation anomaly (mm day⁻¹) for 2013 with respect to the 1998–2012 average.

In the westernmost monsoon-dominated sector of Fig. 4.30 (120°–150°E), some pronounced seasonal rainfall anomalies occur. In the southern monsoon period of January–March 2013 (Fig. 4.30a), rainfall did not penetrate as far south as usual, producing substantial dry conditions south of about 13°S (northeastern Australia). During July–September (Fig. 4.30c), rainfall over the Maritime Continent region was enhanced by about 30% over its climatological value between about 5°N and 5°S. The wetter conditions coincided with higher-than-usual SSTs around Indonesia and the Philippines. In September, an active period of TC formation began, culminating in Super Typhoon Haiyan in November.

The SPCZ exhibited generally higher rainfall intensities than normal, especially in the second half of 2013 (180°–150°W sector in Figs. 4.30c,d, and Fig. 4.31). Figure 4.31 also shows that SPCZ convection was particularly vigorous along 10°S east of the dateline. However, the convective activity seemed to split into two parts to the east of Fiji. Rainfall was above normal for the year over and south-southeast of Fiji (18°S, 175°E), but south of 15°S and east of about 160°W there was an extensive drier-than-normal region. This set-up caused strong contrasts in rainfall across the South Pacific Islands. Thus, Tonga (10° east of Fiji) and the Marquesas Islands in the northern part of French Polynesia were generally wetter than normal through much of 2013, whereas many dry months were experienced in central and southern French Polynesia (<http://www.niwa.co.nz/climate/icu>).

Figure 4.30d for the 180°–150°W sector also suggests that the SPCZ during October–December was equatorward of its normal position, which seems surprising for an ENSO-neutral season. Figure 4.32, which shows south–north rainfall transects for each of the 16 years available from TRMM archive, clarifies the interpretation. In this season, the latitude of

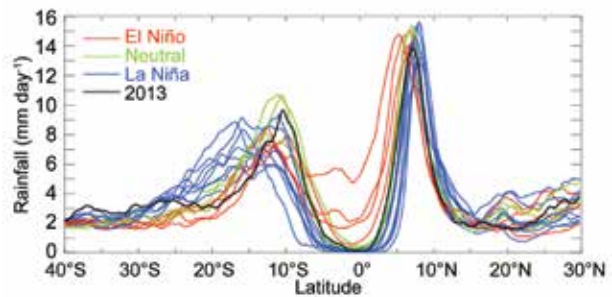


FIG 4.32. TRMM-3B43 rainfall rate (mm day⁻¹) for Oct–Dec period for each year 1998 to 2013, averaged over the longitude sector 180°–150°W. The cross-sections are color coded by ENSO phase according to NOAA’s ONI, except for 2013 (ENSO-neutral) shown in black.

the SPCZ rainfall peak tends to be similar in both ENSO-neutral and El Niño years, although rainfall decreases more sharply poleward of this maximum during El Niño years; however, La Niña years have the peak rainfall displaced significantly poleward, and so drag the climatological peak southwards as well. Thus, Fig. 4.32 shows both ITCZ and SPCZ peak rainfalls align well with the observed locations of other ENSO-neutral years.

2) ATLANTIC—A. B. Pezza and C. A. S. Coelho

The Atlantic ITCZ is a well-organized convective band that oscillates approximately between 5°–12°N during July–November and 5°N–5°S during January–May (Waliser and Gautier 1993; Nobre and Shukla 1996). Equatorial Kelvin waves can modulate the ITCZ interannual variability and ENSO is also known to influence it on the seasonal time scale (Münich and Neelin 2005). In 2013, the prevailing scenario was that of weak negative sea surface temperature anomalies in the equatorial Pacific near the South American coast associated with neutral ENSO conditions, with no clear teleconnective forcing driving the behavior of the Atlantic ITCZ (Fig. 4.33). However, the intra-seasonal activity within the Atlantic sector responded to the typical “seesaw” mechanism between the hemispheres in terms of water temperature and anomalous horizontal divergence, as exemplified in March by an ITCZ well to the north of its climatological position (following the warm water in the North Atlantic) and corresponding suppressed convection on the eastern Amazon and northeastern Brazil (Figs. 4.34 and 4.35).

Based on the local influences outlined above, the year could be divided into January–May as a predominantly dry period in the eastern Amazon and northeastern Brazil, and into June–December as a moderately wet period (Figs. 4.34a,b). In June/July, the positive anomalies to the north of the equator

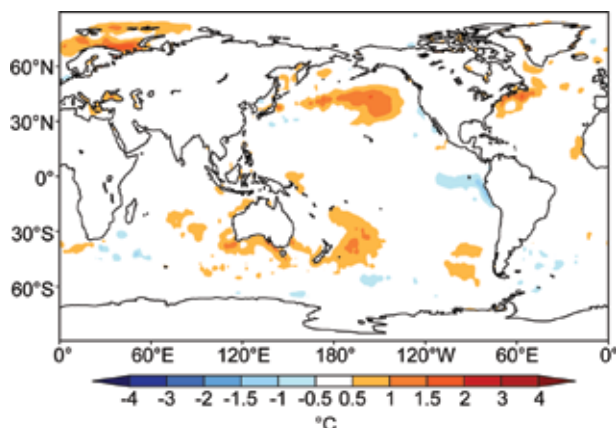


FIG 4.33. Spatial distribution of average global sea surface temperature anomalies (°C, Reynolds et al. 2002) during 2013.

somewhat dissipated (see the partial reversal of the Atlantic Index, Fig. 4.35b), reducing the subsidence forcing on the Brazilian coast and hence helping explain the more favorable rainfall pattern in the second half of the year. The historical interplay of the SST gradient between the South and the North Atlantic is well depicted by the aforementioned Atlantic Index (Fig. 4.35b), which shows a predominance of negative conditions (unfavorable for convection within the South Atlantic ITCZ) over the last few years.

h. Atlantic warm pool—C. Wang

The Atlantic warm pool (AWP) is a large body of warm water in the lower latitudes of the North Atlantic Ocean, comprising the Gulf of Mexico, the Caribbean Sea, and the western tropical North Atlantic (Wang and Enfield 2001, 2003). Previous studies have shown that the AWP plays an important role in Atlantic TC activity, and provides a moisture source for North America, and thus affects rainfall

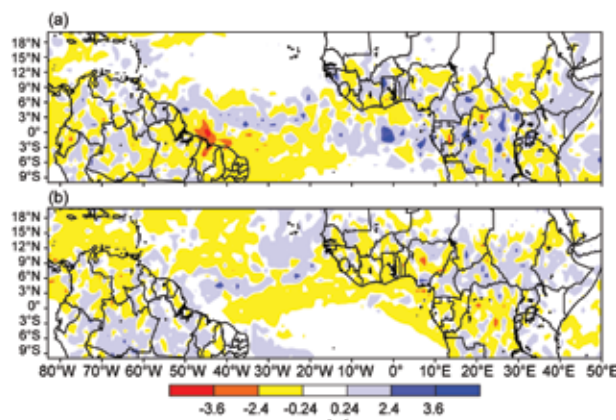


FIG. 4.34. TRMM tropical South America precipitation anomalies (mm hr⁻¹) with respect to 1998–2012 for (a) Jan–May 2013 and (b) Jun–Dec 2013.

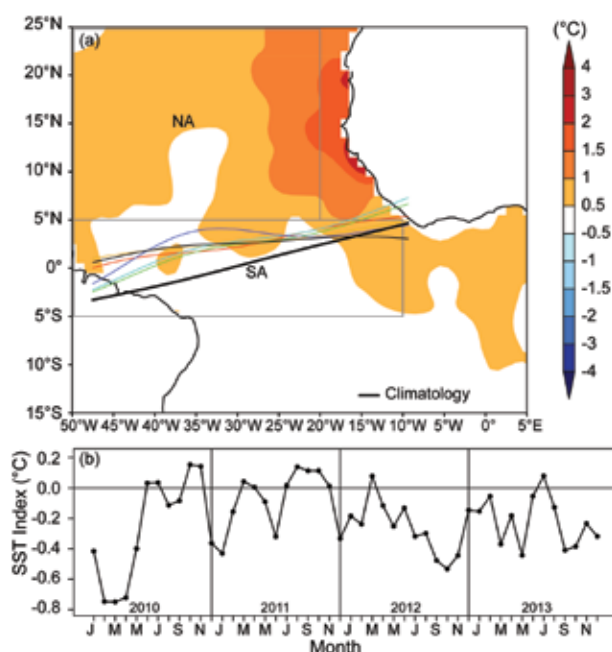


FIG. 4.35. (a) Atlantic ITCZ position inferred from outgoing longwave radiation during Mar 2013. The colored thin lines indicate the approximate position for the six pentads of Mar 2013. The black thick line indicates the Atlantic ITCZ climatological position. The SST anomalies (Reynolds et al. 2002) for Mar 2013 based on the 1982–2012 climatology are shaded. The two boxes indicate the areas used for the calculation of the Atlantic Index in 4.35b; (b) Monthly SST anomaly time series averaged over the South American sector (SA region, 5°S–5°N, 10°W–50°W) minus the SST anomaly time series averaged over the North Atlantic sector (NA region, 5°N–25°N, 20°W–50°W) for the period 2010–13 forming the Atlantic Index. The positive phase of the index indicates favorable conditions for enhanced Atlantic ITCZ activity.

in the central United States (Wang et al. 2006, 2008a, 2011; Drumond et al. 2011). Unlike the Indo-Pacific warm pool, which straddles the equator, the AWP is normally north of the equator. Another unique feature of the AWP is that it does not exist in the boreal winter if the AWP is defined by SSTs warmer than 28.5°C (Wang and Enfield 2001). In addition to the large seasonal cycle, AWP variability occurs on both interannual and multidecadal timescales and has exhibited a long-term warming trend (Wang et al. 2006, 2008b). Figures 4.36a,b depict the long-term total and detrended June–November (JJASON) AWP area indices. The multidecadal and interannual variations of the AWP are displayed in Figs. 4.36c,d respectively.

The multidecadal variability (Fig. 4.36c) shows that the AWP were larger during the period 1930–60, as well as after the late 1990s; and smaller during 1905–25 and 1965–95. The periods for large and small

SIDEBAR 4.1: THE 2013 ATLANTIC HURRICANE SEASON: BLIP OR FLIP?—C. T.

Fogarty and P. Klotzbach

The 2013 Atlantic hurricane season threw a few “curve balls” for forecasters and was the “wild pitch” that triggered lengthy discussions among weather and climate scientists. What was predicted to be a very active season with at least seven hurricanes (about one-third of those projected to be major hurricanes) turned out to produce only two Category 1 hurricanes and just 20% of the predicted ACE. It was the quietest Atlantic hurricane season since 1994 in terms of major hurricanes (none), since 1983 in terms of ACE, and since 1968 for lowest peak intensity of the season’s strongest storm.

Signals that convinced long-range forecasters to anticipate a very active season included anomalously-warm SSTs in the MDR, the absence of El Niño conditions, below-normal sea level pressures in the tropical Atlantic, and persistence of the positive phase of the AMO (Schlesinger and Ramankutty 1994) early in 2013, among other predictors. During neutral or negative phases of ENSO, upper-level wind shear in the tropical Atlantic is generally relatively weak. Neutral ENSO conditions were correctly predicted to be present by most forecast models during the 2013 hurricane season. The expectation that neutral ENSO conditions and a positive phase of the AMO would continue was key to the prediction of at least three major hurricanes—a relationship described by Klotzbach and Gray (2008).

The big question coming out of the season was “why so little activity when most standard pre-season predictors indicated favorable storm formation conditions?” The primary clue was found over the eastern tropical Atlantic and within the MDR where the peak of the season was characterized by enhanced subsidence. Additionally, SSTs evolved in an unusual manner with little warming in the MDR during the spring and first half of summer when surface water should be warming. While tropical Atlantic SSTs were warmer than normal, cool anomalies were evident in the subtropical eastern Atlantic during the early part of the hurricane season (Fig. SB4.1b). This area has been shown in several studies including Klotzbach (2011), to be a critical area for Atlantic hurricane activity. Cold anomalies in this region tend to generate stronger-than-normal baroclinicity, thereby contributing to cold upper-level lows, which enhance African easterly wave recurvature in the eastern part of the basin.

A similar pattern evolved in the higher latitudes of the North Atlantic. This evolution signalled what would be a short-term reversal of the longer-term positive phase of the AMO since the mid-1990s. These observations,

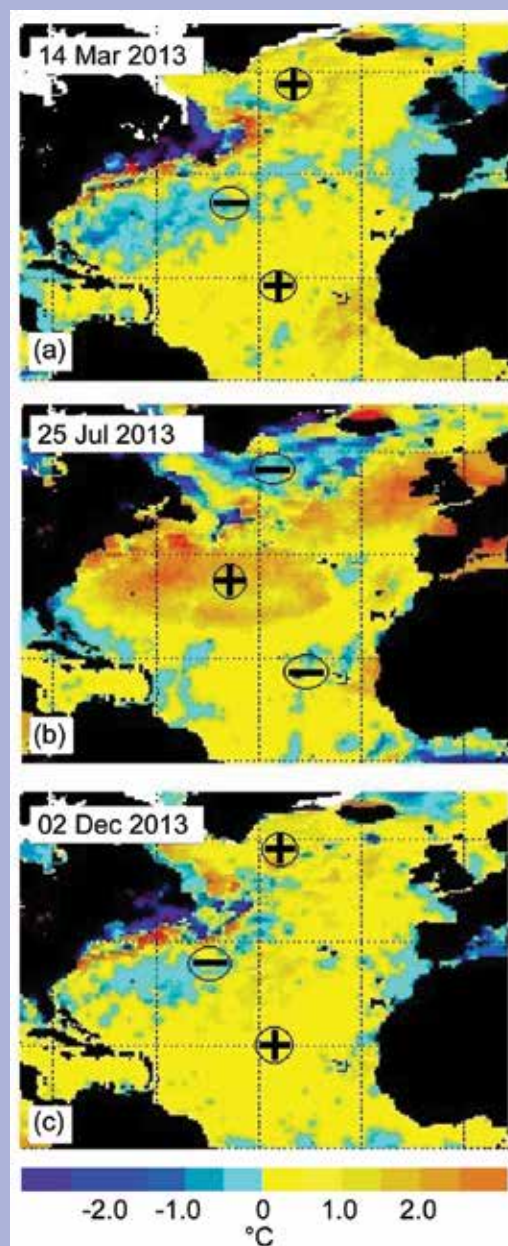


FIG. SB4.1. NOAA/NESDIS 50-km mean weekly SST anomaly (°C) for (a) 14 Mar, (b) 25 Jul, and (c) 02 Dec 2013.

however, raise more questions. Were the enhanced subsidence in the MDR and the “flat-lined” SST (see Fig. SB4.2) related? It certainly appears that way, given that the trade winds strengthened during that period which in turn arrested the usual warming of surface waters necessary to promote convective cloud formation. Dry air from the Saharan region was also advected into the MDR

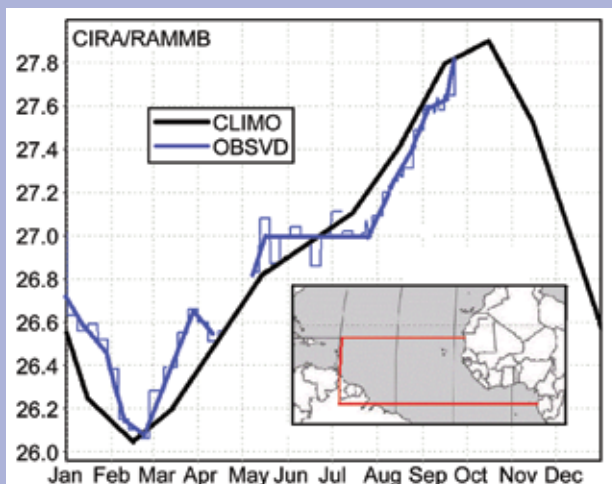


FIG. SB4.2. CIRA/RAMMB area-averaged SST throughout the MDR during 2013. Climatological values shown in black and observed shown in blue. Note the anomaly reversal from May to July.

by the enhanced trade winds. Another source of dry air (and wind shear) appeared to be from numerous cyclonic eddies diving southward during a commensurate reversal of the North Atlantic Oscillation (NAO) from negative to positive. Enhanced subsidence implies weaker easterly waves in the eastern Atlantic and a reduced likelihood of TC formation. Although convection was plentiful over the western part of the basin, above-normal vertical wind shear squelched the development of many storms that attempted to form there. Mid-tropospheric subsidence was also detected over the MDR (see <http://typhoon.atmos.colostate.edu/>).

From August to October the SST anomaly and AMO states returned to their early spring pattern almost as quickly as they deviated early in the year (the similarity between SST anomaly structures in Figs. SB4.1a and c is quite remarkable); however, it appears there was a lagged storm-suppressing impact that affected the MDR during the midst of the season. This intraseasonal change is a reminder that sometimes predictability may be limited to a shorter timeframe, and in the future sudden changes to the AMO cycle (or perhaps even the NAO) may serve as a shorter-term predictor within the season.

Two important questions remain: (1) Does potential exist to anticipate these sudden changes in the AMO? (2) Could the behavior in 2013 simply be a harbinger of a “flip” in the phase of the AMO

from the current positive state to a negative one? The last time such a quiet season occurred was in 1994, at the end of the previous long-term negative phase of the AMO. There can be occasional “blips” in the phase or magnitude of the oscillation as seen in Fig. SB4.3. In 1968 there was a sharp drop in storm activity corresponding to a “dip” in the AMO index during that generally active era; however, the following year was extremely active. Data covering the past ~150 years of hurricane activity in the North Atlantic indicate that a period of ~60 years can be expected between peaks of hurricane activity, so the current active phase is more likely than not to persist for at least a few more years.

In summary, while many of the large-scale conditions typically associated with active TC seasons in the Atlantic were present (e.g., anomalously warm tropical Atlantic, absence of El Niño conditions, anomalously low tropical Atlantic sea level pressures), very dry midlevel air combined with midlevel subsidence and stable lapse rates to significantly suppress the 2013 Atlantic hurricane season. These unfavorable conditions were likely generated by a significant weakening of the strength of the AMO/Atlantic thermohaline circulation during the late spring and into the early summer. This very dry midlevel air is well-illustrated in Fig. 27 from last year’s TC forecast verification report that shows the relative humidity anomalies at 600 hPa; that report is available at <http://hurricane.atmos.colostate.edu/Forecasts/2013/nov2013/nov2013.pdf>.

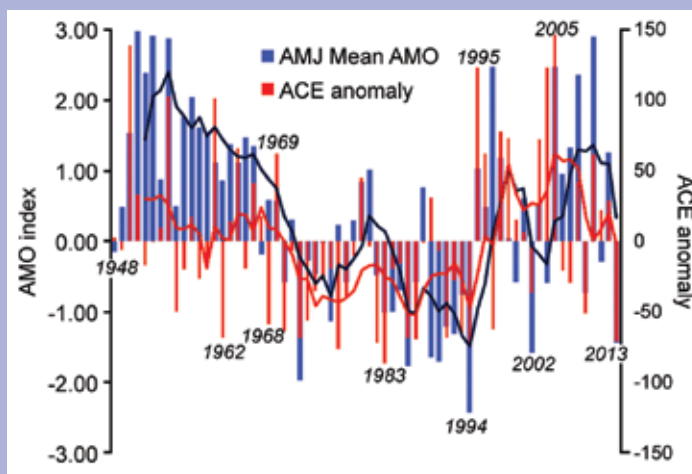


FIG SB4.3. Apr–Jun (AMJ) mean of the AMO and season-total ACE anomaly from 1948 to 2013. Five-year running mean indicated with bold lines.

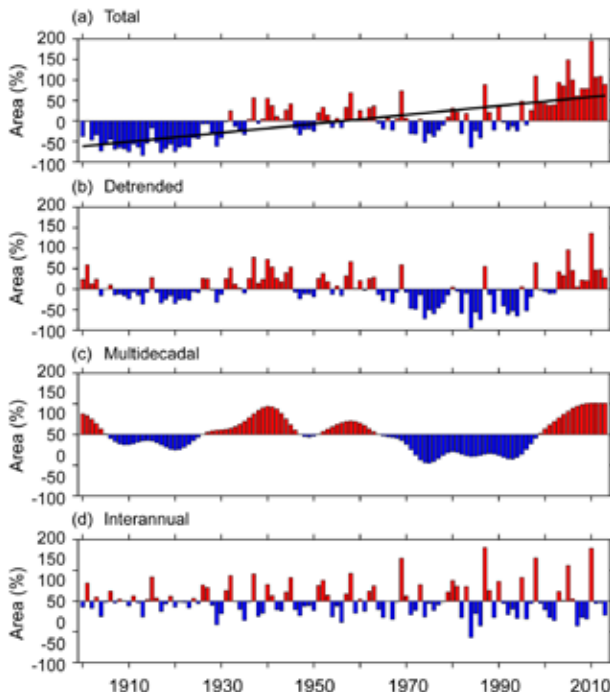


FIG. 4.36. The AWP index from 1900–2013. The AWP area index (%) is calculated as the anomalies of the area of SST warmer than 28.5°C divided by the climatological Jun–Nov AWP area. Shown are the (a) total, (b) detrended (removing the linear trend), (c) multidecadal, and (d) interannual area anomalies. The multidecadal variability is obtained by performing a seven-year running mean to the detrended AWP index. The interannual variability is calculated by subtracting the multidecadal variability from the detrended AWP index. The black straight line in (a) is the linear trend that is fitted to the total area anomaly. The extended reconstructed SST data set is used.

AWPs coincide with the warm and cool phases of the Atlantic multidecadal oscillation (AMO; Delworth and Mann 2000; Enfield et al. 2001). That is, AWP variability is tied to simultaneous alterations of SST in the high latitudes of the North Atlantic in a mode that operates primarily on a multidecadal timescale. Wang et al. (2008b) showed that the influences of the AMO on TC activity and climate might operate through the atmospheric changes induced by the AWP. The interannual AWP variability reflects both the local oceanic/atmospheric processes and the remote delayed influence of Pacific ENSO. The JJASON AWP interannual index of Fig. 4.36d is significantly correlated with the prior December–February (DJF) Niño3 region of SST anomalies, indicating a delayed ENSO effect on the AWP (Wang et al. 2008b). A recent study showed that the equatorial Amazon rainfall during the austral summer is negatively related to the following boreal summer’s AWP SST, manifesting the remote ENSO impact on the AWP SST through

its modulation of the Amazon rainfall (Misra and DiNapoli 2013). However, the contemporaneous correlation of the JJASON Niño3 SST anomalies and JJASON AWP index is not statistically significant. This reflects the facts that (1) large/small AWP in the summer and fall have no clear relation to contemporaneous El Niño/La Niña development, and (2) by the summer and fall of the following year the Pacific El Niño/La Niña anomaly has almost always disappeared.

The AWP was larger than its climatological mean each month in 2013, with the largest AWP occurring in September (Fig. 4.37a). The AWP usually appears in May and peaks in September; however, the 2013 AWP variation was unique as it appeared early in March with a second peak in April. A new study demonstrates that the onset date of the AWP during 1979–2012 ranged from late April to early August (Misra et al. 2014). This indicated that the early onset of the 2013 AWP in March was the earliest onset during the recent decades. Because SSTs were warmer than 28.5°C in the equatorial western Atlantic from March 2013 (Fig. 4.37c), the AWP started to appear in March. In April, the warmer water in the equatorial western Atlantic further developed and merged with the warmer water in the equatorial eastern Atlantic (Fig. 4.37d). By May, the warmer water decayed in the equatorial western Atlantic (Fig. 4.37e). As in previous years, the AWP started to develop in June between the Gulf of Mexico and Caribbean Sea with the 28.5°C SST almost overlapped with the climatological AWP (Fig. 4.37f). By July and August, the AWP was well developed in the Gulf of Mexico and Caribbean Sea and reached eastward to the western tropical North Atlantic (Figs. 4.37g,h). By September, the AWP had further expanded southeastward and the isotherm of 28.5°C covered almost the entire tropical North Atlantic (Fig. 4.37i). The AWP started to decay after October when the waters in the Gulf of Mexico began cooling (Figs. 4.37j,k).

Previous studies have shown that AWP variability affects the Atlantic hurricane tracks (Wang et al. 2011). An eastward expansion of the AWP tends to shift the focus of cyclogenesis eastward, therefore decreasing the probability for hurricane landfall in the southeastern United States. A large AWP also weakens the North Atlantic subtropical high and produces the eastward TC steering flow anomalies along the eastern seaboard of the United States. Due to these two mechanisms, hurricanes are generally steered toward the north and northeast during a large AWP year. The TC steering flow anomalies in 2013

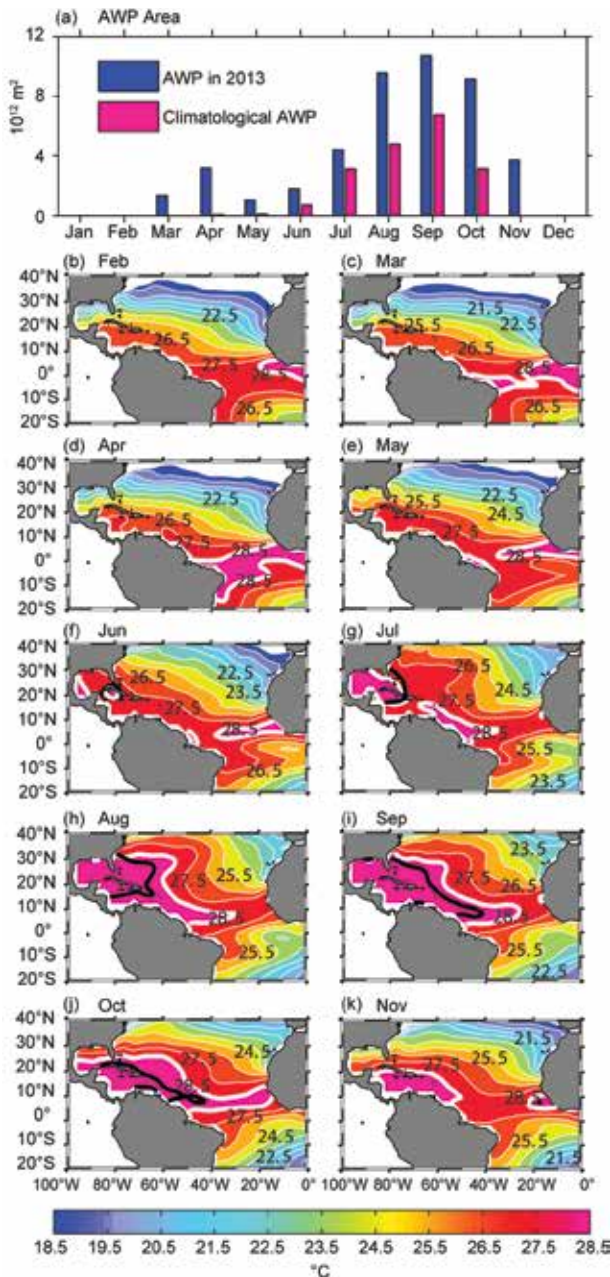


FIG. 4.37. (a) The monthly AWP area in 2013 (10^{12} m²; blue) and the climatological AWP area (red) and the spatial distributions of the 2013 AWP in (b) Feb, (c) Mar, (d) Apr, (e) May, (f) Jun, (g) Jul, (h) Aug, (i) Sep, (j) Oct, and (k) Nov. The AWP is defined by SST larger than 28.5°C. The black thick contours in (f)–(k) are the climatological AWP based on the data from 1971–2000 and the white thick contours are the 2013 28.5°C SST. The extended reconstructed SST data set is used.

were consistent with those of the observed large AWP years (Wang et al. 2011).

During the 2013 Atlantic TC season, the TC steering flow anomalies were characterized by an anomalous cyclone and an anomalous anticyclone

(Fig. 4.38). Associated with these patterns were mostly the eastward and southeastward flow anomalies in the western tropical North Atlantic, and the northward and northeastward flow anomalies in the open ocean of the North Atlantic. An exception was in November during which the TC steering flow anomalies were westward in the hurricane MDR (Fig. 4.38f), but only one storm, Melissa, formed southeast of Bermuda during that month. The distribution of the 2013 TC steering flow was unfavorable for TCs to make landfall in the southeastern United States. While a large AWP is consistent with the fact that no storms made landfall in the southeastern United States in 2013 (either by decaying or moving northward or northeastward), the AWP had no apparent enhancing effect on the number of TCs for the North Atlantic TC season (section 4d2) as a large AWP typically results in more TCs (Wang et al. 2006).

i. Indian Ocean dipole—J.-J. Luo

Interannual climate variability in the tropical Indian Ocean (IO) is driven either by local ocean-atmosphere interactions or by the Pacific ENSO in the presence of interbasin interactions (e.g., Luo et al. 2010). The Indian Ocean dipole (IOD) is one major internal climate mode in the IO that may induce considerable climate anomalies in many countries surrounding the IO. The IOD normally starts in boreal summer, peaks in Northern Hemisphere fall, and declines rapidly in early boreal winter. During May–September 2013, a negative IOD (nIOD) event occurred, characterized by anomalous SST warming in the tropical eastern IO and cooling in the west. Compared to previous events in 1990, 1992, 1996, 1998, 2001, 2005, and 2010 (Luo 2011), the 2013 nIOD was short-lived and weak with warming anomalies in the eastern IO of <0.5°C and a maximum cooling anomaly in the west of about -0.4°C in July (Fig. 4.39). The east warming/west cooling SST dipole structure is linked with stronger-than-normal surface westerlies in the central equatorial IO (Ucio) as noted in Fig. 4.39b; and this is reminiscent of the canonical air-sea coupled feature of nIOD. Note that this nIOD signal occurred along with a weak cooling condition in the Pacific. Such co-occurrence of IOD and ENSO has been found often in the historical records.

SSTs in major parts of the tropical IO during 2013 were warmer than normal except the western IO during June–August (Fig. 4.40). This may be partly due to the rapid rise of the IO SST over past decades in response to increasing greenhouse gas emissions (Hoerling et al. 2004). The fast surface warming in

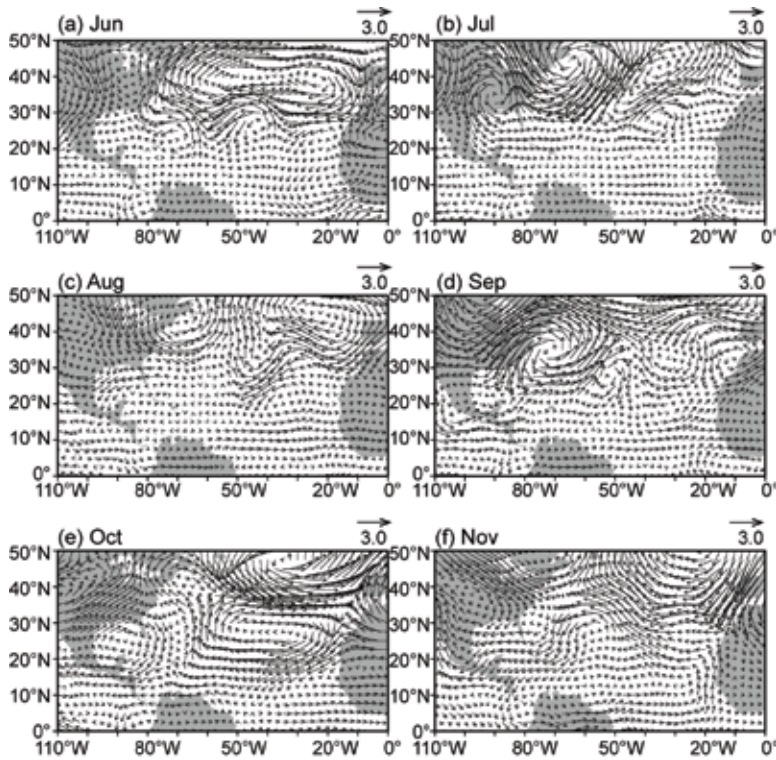


FIG. 4.38. The TC steering flow anomalies in the 2013 Atlantic hurricane season of (a) June, (b) July, (c) August, (d) September, (e) October, and (f) November. The TC steering flow anomalies are calculated by the vertically-averaged wind anomalies from 850 hPa to 200 hPa relative to the climatology of 1971–2000. The NCEP–NCAR reanalysis field is used.

the IO was found to play a key role in generating a La Niña-like climate regime shift in the Pacific by inducing excessive easterlies in the western-central Pacific via modifying the Walker Cell (Luo et al. 2012), and hence may have contributed to the weak cooling condition and stronger-than-normal easterly trade winds in the Pacific throughout 2013. Anomalous easterlies in the western central Pacific and westerlies in the IO converged in

the Indonesia area, in association with the persistent surface warming in the eastern IO and La Niña-like cooling in the Pacific. This induced stronger-than-normal rainfall in the eastern IO–western Pacific during 2013, which is superimposed with active intraseasonal oscillations (Fig. 4.40). Strong westerly bursts occurred in the Ucio during January, May, August, and December in association with the occurrence of eastward-propagating intraseasonal oscillations (Fig. 4.39b). These intraseasonal westerly winds forced noticeable oceanic downwelling Kelvin waves and generated subsurface warming in the eastern equatorial IO (Fig. 4.41a). Note that despite the stronger-than-normal westerlies during late 2012 to early 2013, SSTs in both the eastern and western IO were above normal; this is likely due to dry conditions and hence more solar radiation heating (Fig. 4.39). The Pacific weak warming condition in late 2012 might also contribute to the tropical IO warming during late 2012 to early 2013.

During March–May 2013, the IO basin-wide SST warming persisted despite the prevailing westerly anomalies (Fig. 4.40b). The basin-wide anomalous westerlies might be ascribed to the persistent upper ocean

warming in the east (and along the west coast of Sumatra) and excessive rainfall over the Maritime Continent, partly in association with the Pacific weak cooling condition. While the westerlies tend to maintain the warming in the east by deepening the ocean thermocline there, the above-normal westerlies in the western IO acted to cool SSTs by enhancing surface evaporation and latent heat loss. This contributed to cold SST anomalies in the west

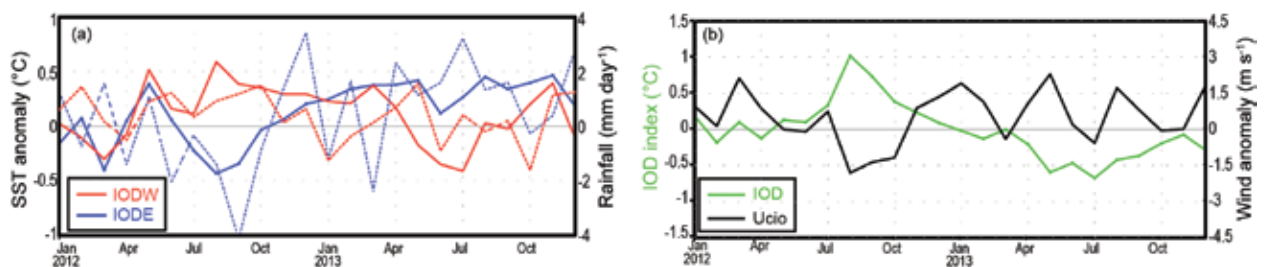


FIG 4.39. (a) Monthly anomalies of SST ($^{\circ}\text{C}$, solid lines) and precipitation (mm day^{-1} , dashed lines) in the eastern (IODE, 10°S – 0° , 90°E – 110°E blue lines) and western pole (IODW, 10°S – 10°N 50°E – 70°E , red lines) of IOD. (b) As in (a), but for the IOD index (measured by the SST difference between IODW and IODE, green line) and surface zonal wind anomaly (m s^{-1}) in the central equatorial IO (Ucio; 5°S – 5°N , 70°E – 90°E , black line). The anomalies were calculated relative to the 1982–2012 climatology. These are based on the NCEP optimum interpolation SST (Reynolds et al. 2010), monthly GPCP analysis (available at <http://precip.gsfc.nasa.gov/>), and JRA-25 atmospheric reanalysis (Onogi et al. 2007).

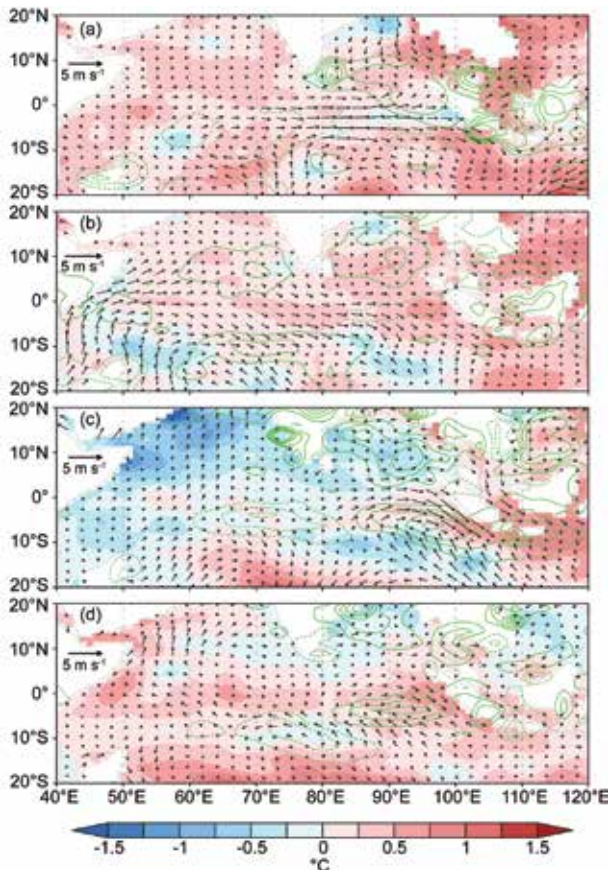


FIG. 4.40. SST ($^{\circ}\text{C}$, colored scale), precipitation (green contour: ± 1 , ± 2 , ..., ± 5 mm day $^{-1}$). Solid/dashed lines denote positive/negative values), and surface wind anomalies during (a) Dec–Feb 2012/13, (b) Mar–May 2013, (c) Jun–Aug 2013, and (d) Sep–Nov 2013.

during May–August. As a result, a negative dipole structure developed during June–August, with dry conditions in the west and excessive rainfalls in the eastern IO (Fig. 4.40). The equatorial westerly anomalies in this season, however, were confined east of 80°E with near-normal winds in the central region, probably owing to intraseasonal disturbances (Figs. 4.39 and 4.40). This suggests that the local air–sea coupling was not strong enough to maintain/enhance the nIOD development. During September–November, the SST warming in western IO rebounded quickly due to reduced cloudiness in that region. Conse-

quently, the negative SST dipole collapsed and basin-wide warming appeared (Fig. 4.40d).

The weak 2013 nIOD appeared to be caused by several factors, including the multidecadal basin-wide warming trend in response to increasing greenhouse gas forcing, active westerly wind bursts related to intraseasonal oscillations, and weak La Niña-like conditions in the Pacific. Additionally, a downwelling Rossby wave in the South IO, primarily driven by anticyclonic wind forcing associated with the positive IOD in late 2012, continuously propagated westward at 12° – 8°S (Fig. 4.41) and may have also contributed to the nIOD in late 2013.

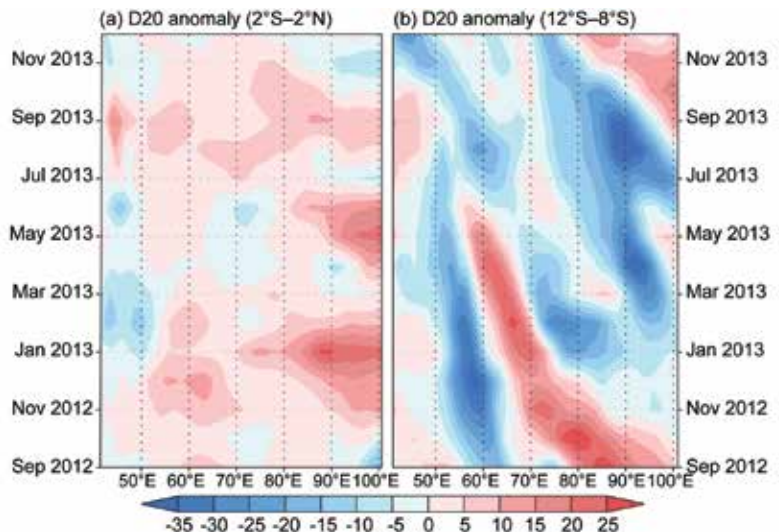


FIG. 4.41. 20°C isotherm depth (D20, m) anomalies in (a) the equatorial Indian Ocean (2°S – 2°N) and (b) off-equatorial South Indian Ocean (12°S – 8°S) in 2013. The data are derived from the NCEP ocean reanalysis available at <http://www.cpc.ncep.noaa.gov/products/GODAS/>.

On the morning of 8 November, Super Typhoon Haiyan (christened “Yolanda” by Philippine authorities; Fig. SB4.4) roared ashore in the Visayas region of the Philippines. This cyclone caused catastrophic destruction and thousands of casualties, particularly within Samar and Leyte Provinces. The city of Tacloban suffered heavy damage from powerful winds and enormous storm surge. The plight of this city became the focus of world media attention and subsequent international relief efforts. The Joint Typhoon Warning Center (JTWC) estimated Haiyan’s one-minute sustained winds at 170 kt (87.5 m s⁻¹) when the storm first touched land in Guiuan in eastern Samar. This preliminary wind speed estimate, which must still be officially validated, would make Haiyan the strongest tropical cyclone at landfall, surpassing the old record of 165 kt (84.9 m s⁻¹) set by Hurricanes Camille (1969) and Allen (1980) in the North Atlantic Basin, and Super Typhoon Tip (1979) in the Western North Pacific. Prior to landfall, the eye of Super Typhoon Haiyan passed directly over Kayangel Atoll, the northernmost island in the Republic of Palau.

Haiyan was the final typhoon of 2013 in the Western North Pacific Basin, forming at a very low latitude south of Pohnpei Island and then proceeding quickly westward in Micronesia. This cyclone became a super typhoon (maximum sustained one-minute winds of 130 kt or 66.9 m s⁻¹) to the east of Palau, just before it tracked directly over Kayangel, causing much destruction but no loss of life. Continuing on a west-northwestward track it made landfall close to the city of Tacloban in Leyte province of the central Philippines. Haiyan was the second super typhoon in less than a year to directly affect the Republic

of Palau and islands in the southern provinces of the Philippines; Super Typhoon Bopha impacted these regions in early December 2012 as noted in Diamond (2013) and Fig. SB4.5.

On 7 November, the JTWC estimated the intensity of Haiyan to be 170 kt (87.5 m s⁻¹), which was the highest wind speed ever assigned to a TC by the JTWC and surpassed the previous record wind speed of 165 kt (84.9 m s⁻¹) assigned to Super Typhoon Tip during October 1979 by 5 kt (2.6 m s⁻¹). The word “assigned” is appropriate because Tip’s 165 kt (84.9 m s⁻¹) peak wind was not actually measured, but was based on a wind-pressure relationship. Haiyan’s 170 kt (87.5 m s⁻¹) peak wind was based on the wind speed equivalent for a Dvorak satellite signature of T8.0 (the highest on the Dvorak scale; Fig. SB4.5). It reached this speed with an impressive and extremely cold cirrus cloud canopy in Fig. SB4.6 (note the extremely cold dark gray shading of the eye wall cloud tops) that was much colder than the Atlantic conditions used to develop the original Dvorak scale (Dvorak 1984). Currently, however, there is no consensus on how to handle the much colder western Pacific tropopause in Dvorak classifications.

While there has not been any storm in recent history as severe as Haiyan to impact Tacloban, there are two documented historical occurrences over 100 years ago of typhoons with similar impact. An intense typhoon in late October 1897 (<http://www.rappler.com/move-ph/issues/disasters/typhoon-yolanda/44062-leyte-1897-typhoon>) was similar to Haiyan in terms of its path, destructive capacity, and very high storm surge. The communities and churches of Samar and Leyte, including Guiuan, Tacloban,

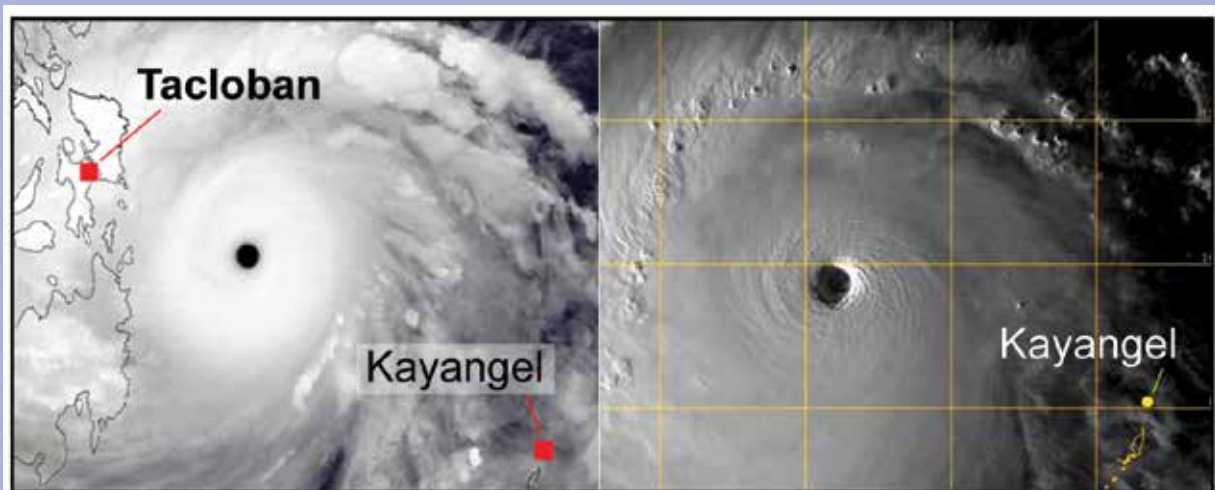


FIG. SB4.4. Super Typhoon Haiyan. Infrared image (left) and visible image (right).

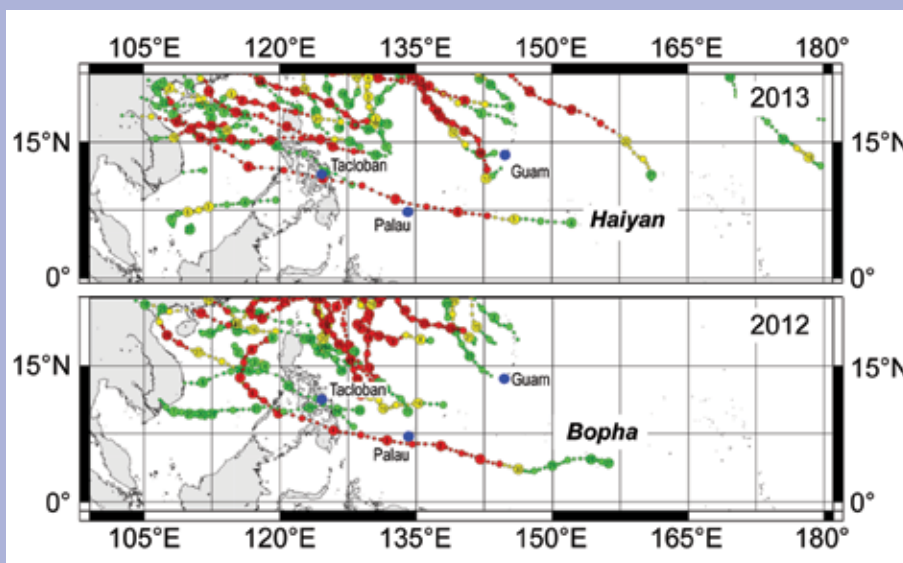


FIG. SB4.5. Tracks of (a) 2013 and (b) 2012 typhoons in the WNP.

and Palo were destroyed and hundreds of residents were killed. Similar to Haiyan, the 1897 typhoon first made landfall near Guiuan in Samar Province, then proceeded to Tacloban. Hernani on the eastern Samar coast experienced a storm surge of 7.3 m, while the storm surge reached 4–5 m in the vicinity of Tacloban.

Another extremely powerful typhoon swept along a path similar to Haiyan in November 1912. The *Washington Herald* issue of 20 November 1912 (<http://www.philstar.com/headlines/2013/11/19/1258482/1912-re->

Haiyan's passage through the Philippine archipelago appears to have been from the accompanying storm surge. A major focus of devastation was on the east coast of Samar and Leyte, with a particular focus on Tacloban. The tremendous storm surge may have been high as 7.5 m, which would make it a candidate for the highest storm surge ever observed in the Philippines and all of East Asia, surpassing the confirmed surge of 7.3 m that struck the Philippines in 1897 (Arafiles and Alcances 1978). Much of the city of Tacloban sits less than 5 m above sea level.

ports-tacloban-storm-killing-15000-resurface) ran a story headlined, “15,000 die in Philippine storm”. It reads, in part: “The typhoon swept the Visayas and is said to have practically destroyed Tacloban, the capital city of Leyte, and to have wrought enormous damage and loss of life at Capiz, ... 15,000 persons were probably killed and wounded in a typhoon ... probably half the population of the two cities had been lost.”

The major cause of damage and loss of life during

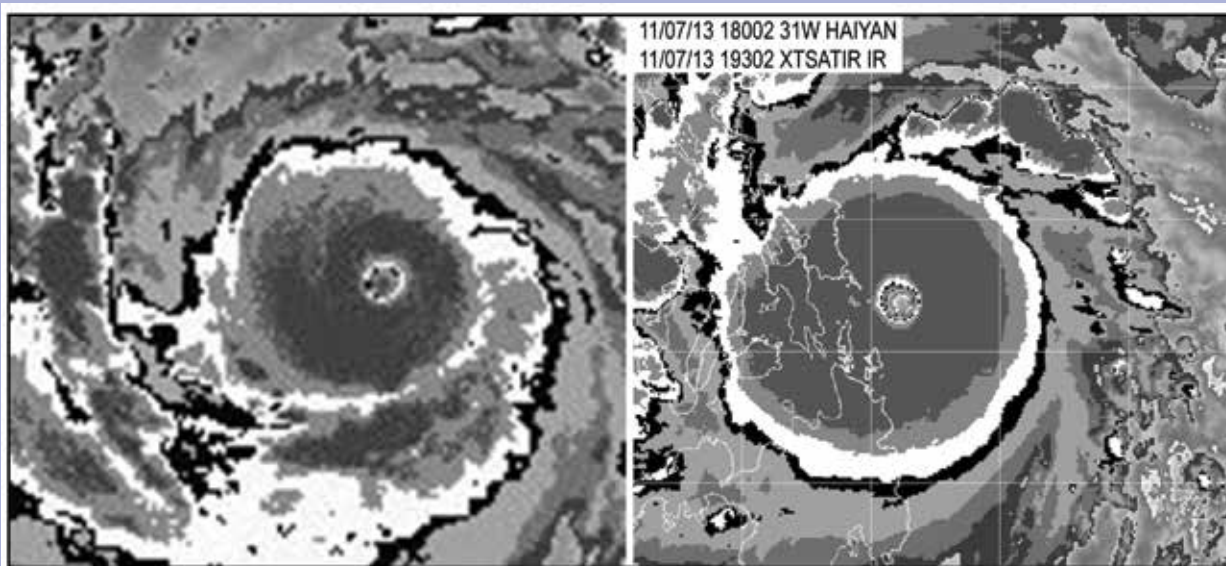
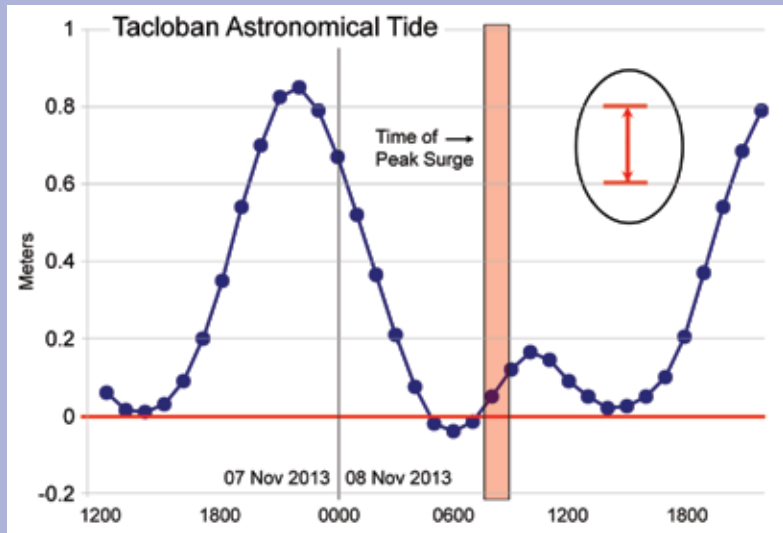


FIG SB4.6. Enhanced infrared images of Typhoons Tip (left) and Haiyan (right) at peak intensities of 165 kt (85 m s⁻¹) and 170 kt, (87 m s⁻¹) respectively. Note the extremely cold dark gray shading of the eye wall cloud tops.

Early surge estimates at Tacloban are 6.5 m at the airport and possibly 8.5–9.1 m in downtown Tacloban. The downtown surge height estimates are based on eyewitness accounts from the iCyclone chase team (<http://www.icyclone.com>).

The surge came rapidly in some locations with nearly the same force and rapidity of a destructive tsunami (e.g., <http://www.youtube.com/watch?v=rS0gv4Xbw7w>). The configuration of the coastline, and its location at the head of San Pedro Bay on the northwest reaches of Leyte Gulf, make Tacloban particularly vulnerable to storm surge. Early modeling results from the Deltares Engineering Group in the Netherlands (e.g., Fig. SB4.7), indicate a surge height of at least 5 m at Tacloban.

The sea level in the region of the central Philippines (and eastward into Micronesia) is currently at historical highs. Since 1970, the mean sea level at Legaspi in the Visayan Island group of the central Philippines has risen by 200 mm. Most of this rise is attributable to an increase of the Pacific trade winds, and not directly tied to the rise of the sea due to climate warming. Regardless of the cause, the 200 mm rise of mean sea level is roughly 20% of the magnitude of the range of the astronomical tide at



Tacloban (Fig. SB4.8). However, the peak surge at Tacloban during Haiyan occurred at a time of relatively low water level. The addition of 200 mm to the low astronomical water level at the time would still have left the water level 0.5 m below the expected high tide for that day.

In summary, Haiyan's extreme intensity and deadly power immediately fueled speculation on the role of climate change in its occurrence and behavior. Haiyan's behavior was unusual on several counts: (1) high intensity at such a low latitude (i.e., $\sim 5^\circ\text{N}$); (2) extreme intensity for the overall basin; (3) record-setting landfall intensity; (4) destructive and deadly power in the Philippines; and, (5) its one-year follow-on to a similar unusual low-latitude intense Typhoon Bopha in 2012. With Haiyan potentially achieving record global typhoon wind intensity, it is likely that a special team will have to be assembled to investigate the legitimacy of this new record and to place Haiyan in its proper ranking among the pantheon of the world's most powerful tropical cyclones.

